SAND2022-9580J

Typological Representation of the Offshore Oceanographic Environment along the Alaskan North Slope

William K. Eymold[1], Christopher Flanary[2], Li Erikson[3], Kees Nederhoff[4], Christopher C. Chartrand[1], Craig Jones[2], Jeremy Kasper[5], and Diana L. Bull[1*]

[1]*Sandia National Laboratories, Albuquerque, NM 87123, USA*
[2]*Integral Consulting Inc., Santa Cruz, CA 95060, USA*
[3]*US Geological Survey (USGS), Pacific Coastal and Marine Science Center, Santa Cruz, CA 95060, USA*
[4] *Deltares USA, 8601 Georgia Ave #508, Silver Spring, MD 20910, USA*
[5]*University of Alaska Fairbanks, Fairbanks, AK 99775, USA*

**Corresponding author*: dlbull@sandia.gov

Abstract

Erosion and flooding impacts to Arctic coastal environments are intensifying with nearshore oceanographic conditions acting as a key environmental driver. Robust and comprehensive assessment of the nearshore oceanographic conditions require knowledge of the following boundary conditions: incident wave energy, water level, incident wind energy, ocean temperature and salinity, bathymetry, and shoreline orientation. The number of offshore oceanographic boundary conditions can be large, requiring a significant computational investment to reproduce nearshore conditions. This present study develops location-independent typologies to reduce the number of boundary conditions needed to assess nearshore oceanographic environments in both a Historical (2007-2019) and Future (2020-2040) timespan along the Alaskan North Slope. We used WaveWatch III®, Delft3D Flexible Mesh, and Delft3D-WAVE model output from six oceanographic sites located along a constant ~50 m bathymetric line spanning the Chukchi to Beaufort Seas. K-means clustering was applied to the energy-weighted joint-probability distribution of significant wave height (H_s) and peak period (T_p). Distributions of wave and wind direction, wind speed, and water level associated with location-independent centroids were assigned single values to describe a reduced order, typological rendition of offshore oceanographic conditions. Reanalysis data (e.g., ASRv2, ERA5, and GOFS) grounded the historical simulations while projected conditions were obtained from downscaled GFDL-CM3 forced under RCP8.5 conditions. Location-dependence for each site is established through the occurrence joint-probability distribution in the form of unique scaling factors representing the fraction of time that the typology would occupy over a representative year. As anticipated, these typologies show increasingly energetic ocean conditions in the future. They also enable computationally efficient simulation of the nearshore oceanographic environment along the North Slope of Alaska for better characterization of coastal processes (e.g., erosion, flooding, or sediment transport).

1. Introduction

Erosion in multiple Arctic locations has increased 1.5 to 4 times in the early 2000's over historic rates (Jones et al., 2018), not only impacting the physical coastline but also driving chemical and biological dynamics (Bristol et al., 2021). Erosion and flooding events have resulted in the relocation of multiple native villages at considerable expense (e.g., villages of: Kivalina (Palinkas, 2020), Shishmaref (Bronen and Chapin, 2013), and Newtok (Ristroph, 2021)). Unfortunately, flooding and erosion risk assessments in Arctic coastal communities that could better inform relocations or adaptations are limited by the availability of high resolution predictive analyses (Melvin et al., 2017). These predictive analyses depend upon accurate representation of the environmental drivers (e.g., atmospheric conditions and oceanographic conditions) as well as the permafrost characteristics (Irrgang et al., 2022). Incident oceanographic conditions of wave energy (via the proxy of open water days) and water level have been shown to exhibit a strong control over erosion and flooding (Barnhart et al., 2014a; Casas-Prat and Wang, 2020a; Günther et al., 2015; Hequette and Barnes, 1990; Overeem et al., 2011). However, the Arctic's remote location, harsh environmental conditions, and relatively low research interest has resulted in limited availability of data related to increased erosional and flooding processes.

To better understand ocean driven nearshore processes in the Arctic such as erosion (e.g., Barnhart et al., 2014a; Ravens et al., 2012), flooding (e.g., Radosavljevic et al., 2016), and sediment transport (e.g., Yager and Ravens, 2013), scientists require accurate predictions of the site-specific long-term nearshore oceanographic conditions (Camus et al., 2011). Accurate prediction of the oceanographic conditions at these local scales necessitates coupled offshore and nearshore (shallow water) models of wave and circulation fields (e.g., WAVEWATCH III® (WW3DG, 2016), Delft3D-FLOW (Deltares, 2018a), and Delft3D-WAVE (SWAN) (Deltares, 2018b)). To develop site-specific conditions nearshore, coastal models require offshore wave and atmospheric conditions (Camus et al., 2011; Stansby et al., 2007), as well as detailed knowledge of the local bathymetry and shoreline orientation. These simulations become computationally expensive due to resolution requirements in the nearshore and the large number of boundary conditions that must be modeled as many years of data are needed to establish reliable estimates.

Despite evidence of some of the fastest changes in oceanographic conditions with the disappearance of Arctic sea ice (Overland et al., 2019; Perovich, 2018) and corresponding increase in open water season and fetch lengths (Barnhart et al., 2014b; Casas-Prat and Wang, 2020b;

Thomson et al., 2016; Thomson and Rogers, 2014), robust and comprehensive assessment of the incident Arctic wave climate is lacking with high fidelity studies only focusing on extreme conditions (Casas-Prat and Wang, 2020a; Casas-Prat and Wang, 2020b)or, more commonly, Arctic researchers searching for simplifications due to the computational expense and level of expertise required in developing nearshore oceanographic conditions. Some of these simplifications circumvent the advanced models altogether. By assuming fetch-limited shallow water wave development, Barnhart et al. (2014b) were able to develop the local wind-driven wave environment at Drew Point, Alaska. Further analytical relationships employing local winds and atmospheric pressure can determine the surge and wave set-up conditions as was done by Barnhart et al. (2014b) and Ravens et al. (2012).

Other simplifications focus on reducing the boundary conditions to a representative subset which can then be used to model nearshore conditions in any modeling framework. For instance, Ravens et al. (2012), chose to increase tractability by modeling only a subset of the wind conditions found through binning into a set of 32 preset classifications. However, selection of a representative subset of boundary conditions can be improved dramatically by applying more sophisticated clustering algorithms as has been done outside of the Arctic region (e.g., Abadie et al., 2006; Bull and Dallman, 2017; Camus et al., 2011; Lavelle and Kofoed, 2013). A comparison of the k-means, self-organizing maps, and maximum dissimilarity algorithms showed that k-means clustering can correctly determine average wave climates (Camus et al., 2011). The k-means clustering of significant wave height (H_s), peak period (T_p, defined as the period with maximum energy in the spectrum), and peak wave direction (D_p) data has been used to elucidate local storm events and characterizations of waves and currents off the coast of France, Latin America, the United Kingdom, and the west coast of the United States (Abadie et al., 2006; Camus et al., 2011; Hegermiller et al., 2017; Reguero et al., 2013). Additionally, data representing the energy occurrence of H_s and T_p from National Data Buoy Center (NDBC) buoys across the Pacific Ocean have been clustered to represent a single set of boundary conditions which are each uniquely scalable to achieve location-specific average annual power flux (Bull and Dallman, 2017).

The goal of the present study is to develop a typological representation of the offshore environment along the Alaskan North Slope consisting of the boundary conditions required for high-resolution nearshore models. Depending upon the methodology employed, up to order 10^4 – 10^5 simulations may be required to represent the environment; an offshore typology is a reduced

number of parameters (order 10) that are prototypical of the full set of parameters needed for nearshore coastal analyses. Inherent in the development of this typology are scaling mechanisms to achieve location-dependent properties to enable community scale analyses. This approach expands analyses from focusing solely on storms (Casas-Prat and Wang, 2020a) by using statistically derived representations of an entire year; this opens the potential for erosion and flooding during more common times of lower oceanic interaction with the coast. To achieve this goal, we modify the k-means clustering approach to obtain location-independent wave energy parameters (H_s, T_p). We then evaluate distributions of other coupled parameters (D_p, water level, wind direction, wind speed, along with regional salinity and temperature values) to account for the full set of needed boundary conditions for nearshore models.

Section 2 identifies the offshore oceanographic and atmospheric data from multiple locations off the North Slope of Alaska used in this analysis during two timespans, Historical (2007-2019) and Future (2020-2040). Section 3 details the methodology by which the Historical and Future offshore typologies are selected while Section 4 details the results of the methodology. Discussion and concluding summary are offered in Sections 5 and 6.

2. Offshore Environment along Alaskan North Slope

2.1. Analysis Sites

We have identified a set of six sites located along the 50 m bathymetric contour off the coast of the North Slope of Alaska (Figure 1). These sites span ~1,250 km and were selected to capture the variation in offshore conditions expected along the North Slope during the ice-free season. While each of these locations will experience site-specific ocean conditions depending on local temperature, salinity, wind, and wave influences throughout each year, we seek prototypical conditions (oceanic and atmospheric) for the Historical and Future timespans that can act as boundary conditions for high-resolution nearshore models. For each site, six geophysical parameters are needed for these boundary conditions; these parameters are H_s, T_p, D_p, water level, wind direction, wind speed, water temperature, and salinity.

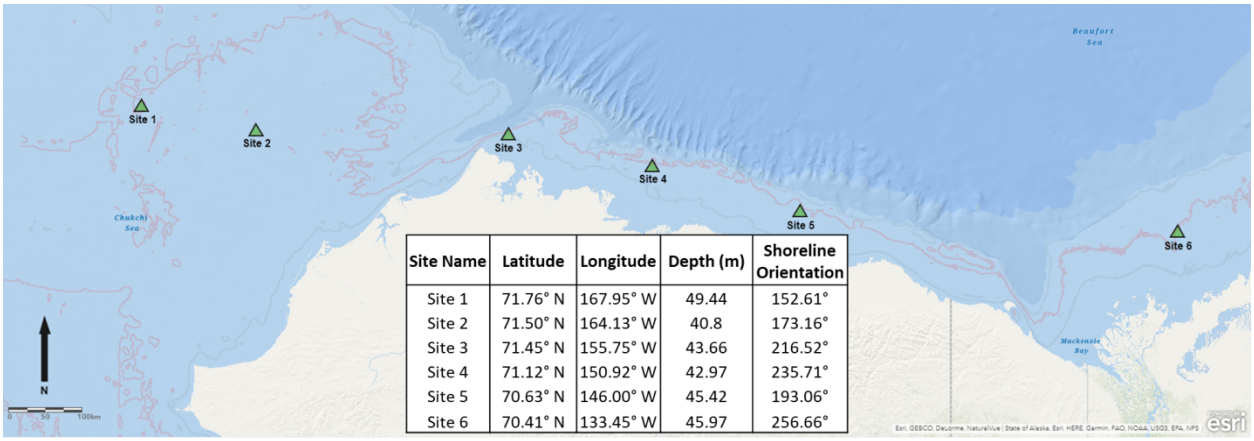

Site Name	Latitude	Longitude	Depth (m)	Shoreline Orientation
Site 1	71.76° N	167.95° W	49.44	152.61°
Site 2	71.50° N	164.13° W	40.8	173.16°
Site 3	71.45° N	155.75° W	43.66	216.52°
Site 4	71.12° N	150.92° W	42.97	235.71°
Site 5	70.63° N	146.00° W	45.42	193.06°
Site 6	70.41° N	133.45° W	45.97	256.66°

Figure 1. Map of sites in study area along North Slope of Alaska. Constant line of 50m bathymetry is shown in red, with 20m and 80m contours shown in gray.

2.2. Modeling Offshore Conditions

2.2.1. Model Setup

We simulate circum-Arctic wave propagation using the spectral wave model WAVEWATCH III® (referred to as WW3) to solve the wave action balance equation explicitly by marching forward in time (WW3DG, 2016). The WW3 model wave grid is polar centric and extends south to 65°N, with a horizontal resolution of 18 km at 70°N (Rogers and Zieger, 2014). The area around the North Pole is masked to avoid complicated computational solutions (singularity issues). Bathymetric data for the model domain were obtained from the ETOPO1 1 arc-minute global relief model (Amante and Eakins, 2009). A spatially varying wavenumber grid is used by WW3 to reduce the loss of model resolution for simulated waves traveling from deep to shallower water, making it advantageous for use in shelf seas like the Arctic Ocean. In our operation of WW3, ice is treated as a solid surface, like an island (i.e., wind is unable to develop waves in the grid cells occupied with ice coverage).

Water level deviations were simulated using an Alaska-centered regional Delft3D Flexible Mesh model (Delft3D FM; Kernkamp et al., 2011). The model is run in depth-averaged barotropic mode assuming that the water density is uniform in both space and time. The computational mesh is unstructured, defined in spherical coordinates and covers an area of 48°-81°N and 159°E-135°W. Model resolution varies with depth and is the coarsest, 10km, in the deepest part of the domain and decreases to 500 m for shallow water while adhering to recommended criteria for smoothness and orthogonality. Wind and pressure forcing is considered across the domain

including the inverse barometer effect (IBE) at the ocean boundaries. Wind stress is based on Garratt (1977) and Lüpkes et al. (2012) which describes the air-sea momentum flux as a function of wind speed and, in contrast to most studies, ice concentration. This ability to incorporate ice fields into the computation of wind drag coefficients is similar to how it is handled by the ADvanced CIRCulation Model for Oceanic, Coastal, and Estuarine Waters (ADCIRC) (Joyce et al., 2019).

2.2.2. Boundary Conditions

An accurate description of the Arctic's oceanographic and atmospheric conditions from observations is not possible due to intermittent or a complete lack of data. Researchers thus rely on reanalysis and modeled data to provide a consistent dataset, available at fixed temporal intervals, that operate as the boundary conditions for other more catered models of desired processes. Here, wind forcing and sea ice boundary conditions for the circum-Arctic WW3 domain were derived from two model reanalyses, the Arctic System Reanalysis v2 (ASRv2) (Bromwich et al., 2018) and the ERA5 reanalysis data (C3S, 2017). ASRv2 is a polar central reanalysis dataset optimized to accurately depict Arctic conditions, while ERA5 is a coarser, global climate reanalysis product from the European Centre for Medium-Range Weather Forecasts.

The circum-Arctic WW3 model simulated wave conditions from July through November for years 2007 – 2019 (Bull et al., 2020); these months were selected as coastal observations at Drew Point, Alaska showed mainly sea-ice free conditions. ASRv2 wind and sea ice data, updated every 3 hours, were used for years 2007 – 2016, based on data availability, and hourly ERA5 wind and sea ice data were used for years 2017 – 2019. These reanalysis datasets were linearly interpolated onto the circum-Arctic WW3 model to provide spatially and temporally varying wind and sea ice forcing (Bull et al., 2020).

ERA5 surface pressure, wind, and ice conditions were also used to simulate the water level deviations in response to the environment in an Alaska centered regional model of Delft3D FM. The model is forced from the ocean boundaries with astronomical conditions based on FES2004 (Lyard et al., 2006). Astronomic tides are computed by applying 31 time and space varying astronomic constituent amplitudes and phases along the open boundaries from the FES2014 tidal loading database (Lyard et al., 2006). Half degree resolution ERA5 winds and atmospheric pressures were applied across the domain at 3 hourly intervals to simulate IBE and wind-driven storm surge.

For both the wave and water level models, Future conditions in the months spanning June – December from 2020 - 2040 were sourced from data prepared by Scenarios Network for Alaska & Arctic Planning (SNAP) (www.snap.uaf.edu; Bieniek et al., 2016). SNAP downscaled the NOAA Geophysical Fluid Dynamics Laboratory Coupled Physical Model (GFDL-CM3; Donner et al., 2011; Griffies et al., 2011) 2-degree global scale climate model forced under Representative Concentration Pathway (RCP) 8.5 for Alaska (Van Vuuren et al., 2011). These downscaled data, updated hourly, yielded more accurate wind, surface pressure, and ice forcing conditions for projected wave and water level simulations. The timeframe for ice cover in the Arctic has been reduced by ~3 days per decade due to earlier melt onset and by ~7 days per decade due to later freeze-up (Stroeve and Notz, 2018). Our shift in analysis from July-November for Historical conditions to June–December for Future conditions therefore explicitly acknowledges that the open-water season length will increase in the future (Barnhart et al., 2014b; Casas-Prat and Wang, 2020b; Meredith et al., 2019).

Skin temperature data over the open ocean, defined as the surface temperature at radiative equilibrium that forms at interfaces between surfaces and the atmosphere (Jin, 1997), from ASRv2 and ERA5 were used to determine Historical water temperature values. Salinity data, updated every 3 hours, were obtained from the GOFS 3.1 global reanalysis and analysis data sets. GOFS combines the Hybrid Coordinate Ocean Model (HYCOM) and the Navy Coupled Ocean Data Assimilation (NCODA) system (Cummings, 2005; Cummings and Smedstad, 2013). Neither water temperature nor salinity data were available for the Future timespan.

2.2.3. Model Outputs

Simulated outputs from WW3 include hourly updates to spectral properties of the sea states. A sea state describes the stochastic process of the sea surface elevation, η, over ~30 minute to 1 hour durations for which stationarity in parameters is assumed (Chakrabarti, 1987; Holthuijsen, 2010; Ochi, 1998). A sea state is typically defined by the frequency spectrum, $S(\omega)$, that accounts for the instantaneous variance of the incoming wave heights (and hence energy) over a range, f, of radial frequencies, ω_f; with H_s and T_p being statistical properties of the spectrum. Hence, WW3 defines the evolving sea states with H_s, T_p, and D_p by assuming a spectral shape and omni-directional waves.

Simulated outputs from Delft3D FM include hourly updates to the water level. Combined with temperature, salinity, and the wind forcing conditions, the WW3 and Delft3D FM modeled

outputs capture the full set of boundary conditions needed for high-resolution nearshore oceanographic models.

There are no sustained oceanographic measurements along the North Slope of Alaska; only sporadic deployments exist, often explicitly for private oil and gas development work, rendering complete validation of oceanographic models in this area infeasible. However, using six measurements spanning 2011-2015, Bull et al. (2020) were able to show that WW3 predicted H_s and T_p, wave conditions derived from ASRv2 forcing data were able to match observational records in depths greater than 20 m with high skill even though H_s above 2 m are underpredicted. Results from Bull et al. (2020) are summarized in Appendix Table A1.

2.3. Statistical Representations of Wave Conditions

Statistically representative wave conditions are often generated by evaluating many years of data to characterize the likelihood of a particular H_s value occurring with a particular value of T_p for a given spectral shape of $S(\omega)$. These scatter diagrams of occurrence (Figure 2) are the foundation of joint-probability distributions (JPD) and enable an annual representation of incident sea states through a probabilistic approach (Ochi, 1998). Occurrence analysis assumes stationarity in the climate over the time period of the analysis. The occurrence values analogously represent the fraction of time the sea state would occupy in a representative year.

More energetic sea states will be more likely to result in damaging conditions along the coast, and hence considerations of energy in the ocean conditions is important. The average annual power flux (AAP) (kW/m) represents the average energy delivered in a year for a given spectral shape and is given by:

$$AAP = \sum JPD(H_s,T_p) * J(H_s,T_p) = \sum_{ij} JPD_{ij} * J_{ij} \quad \text{(Equation 1)}$$

where the power flux J_{ij} (kW/m) for each sea state is given by:

$$J(H_s,T_p) = J_{ij} = \sum_f \rho g c_{g,f} S_{ij}(\omega_f) \Delta\omega_f \quad \text{(Equation 2)},$$

and where ρ is the density of water, g is gravity, ij to the specific sea state (H_s,T_p pair), and $c_{g,f}$ is the group velocity obtained through the dispersion relationship (see Holthuijsen (2010) for more information regarding linear wave theory). In Alaska, the standard Joint North Sea Wave Observation Project (JONSWAP) spectral shape is likely the most suitable spectrum as it was developed from North Sea wave data; it is used here with a γ value of 3.3 to calculate AAP at each of the sites (see Chakrabarti (1987) or Ochi (1998) for more information regarding standard spectral shapes).

For many applications, the energy-weighted occurrence of sea states is typically preferred over frequency of occurrence as more energetic sea states often define the degree of erosion (e.g., Barnhart et al., 2014a), the amount of flooding (e.g., Bilskie et al., 2014), or design criteria for wave energy converters (WEC) (e.g., Cahill and Lewis, 2013; Dallman and Neary, 2014). While both the occurrence and energy contributions are important for this study, the most frequent sea states do not always contribute the most energy to the AAP at each site (Cahill and Lewis, 2013; Lenee-Bluhm et al., 2011). The energy-weighted occurrence, ζ_{ij}, scales each occurrence value, JPD_{ij}, by the energy in that sea-state, J_{ij}, and is then normalized by the AAP:

$$\zeta_{ij} = \frac{JPD_{ij} \times J_{ij}}{AAP} \text{ or } \zeta_{ij} = \frac{JPD_{ij} \times J_{ij}}{\sum_{ij} JPD_{ij} J_{ij}} \quad \text{(Equation 3).}$$

The process of evaluating the energy-weighted occurrence results in longer wavelength, higher amplitude waves becoming more important.

Using the Historical and Future modeled oceanographic conditions, H_s – T_p scatter diagrams of occurrence and energy-weighted occurrence were generated; an example comparison for the Historical and Future values at Site 4 is shown for occurrence (Figure 2) and energy-weighted occurrence (Figure 3). The Historical data were composed of 47,736 samples while 73,568 samples comprised the Future data (noting that the Future open water season had two extra analysis months every year and lasted for an additional seven years). Note, that if these samples were used directly ~700,000 simulations would be required in the nearshore. By binning each sample into a sea state (H_s – T_p pair) and tallying occurrence (or energy-weighted occurrence), a statistically representative year of expected conditions is generated requiring ~200 simulations. Note, every sea state with a numerical value in Figures 2 & 3 indicates that WW3 modeled a condition representative of that sea state. The Future data include several gaps in coverage where simulations did not complete (e.g., August 2025, 2032, 2039; September 2022, 2029, 2036; December 2028), but all sites have identical data coverage and allow for a consistent analysis across the study area. Historical and Future scatter diagrams of occurrence and energy-weighted occurrence for the other five sites are presented in the Appendix (Figures A1 – A10).

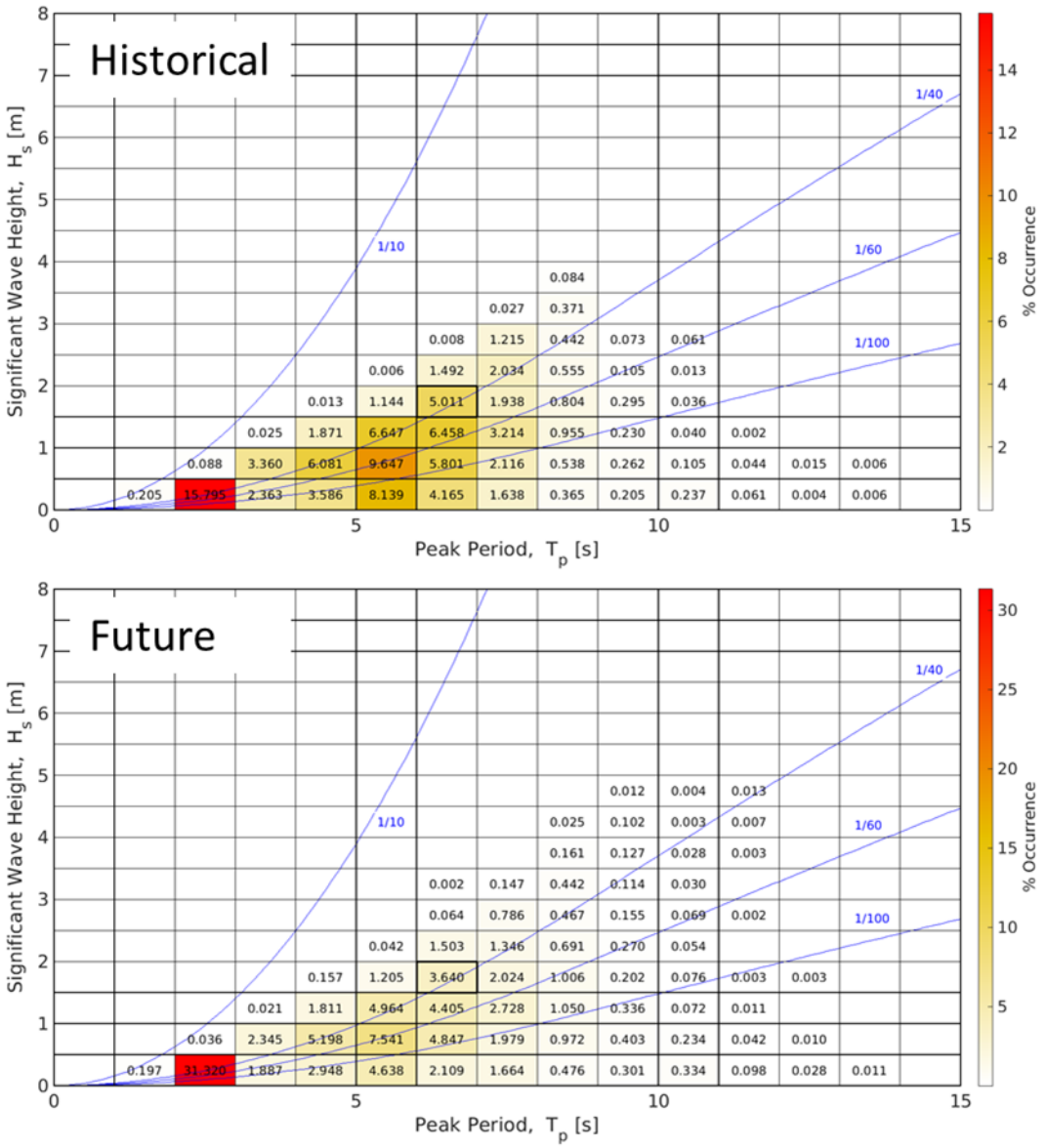

Figure 2. Occurrence JPD at the Site 4 for (top) Historical (2007-2019) and (bottom) Future (2020-2040) time periods. Blue lines indicate constant inverse steepness curves (steepness = λ_{Tp}/H_s, where λ_{Tp} is the wavelength of the peak period). Occurrence is represented both numerically and through color and is used to determine the time apportionment of each cluster in an average year.

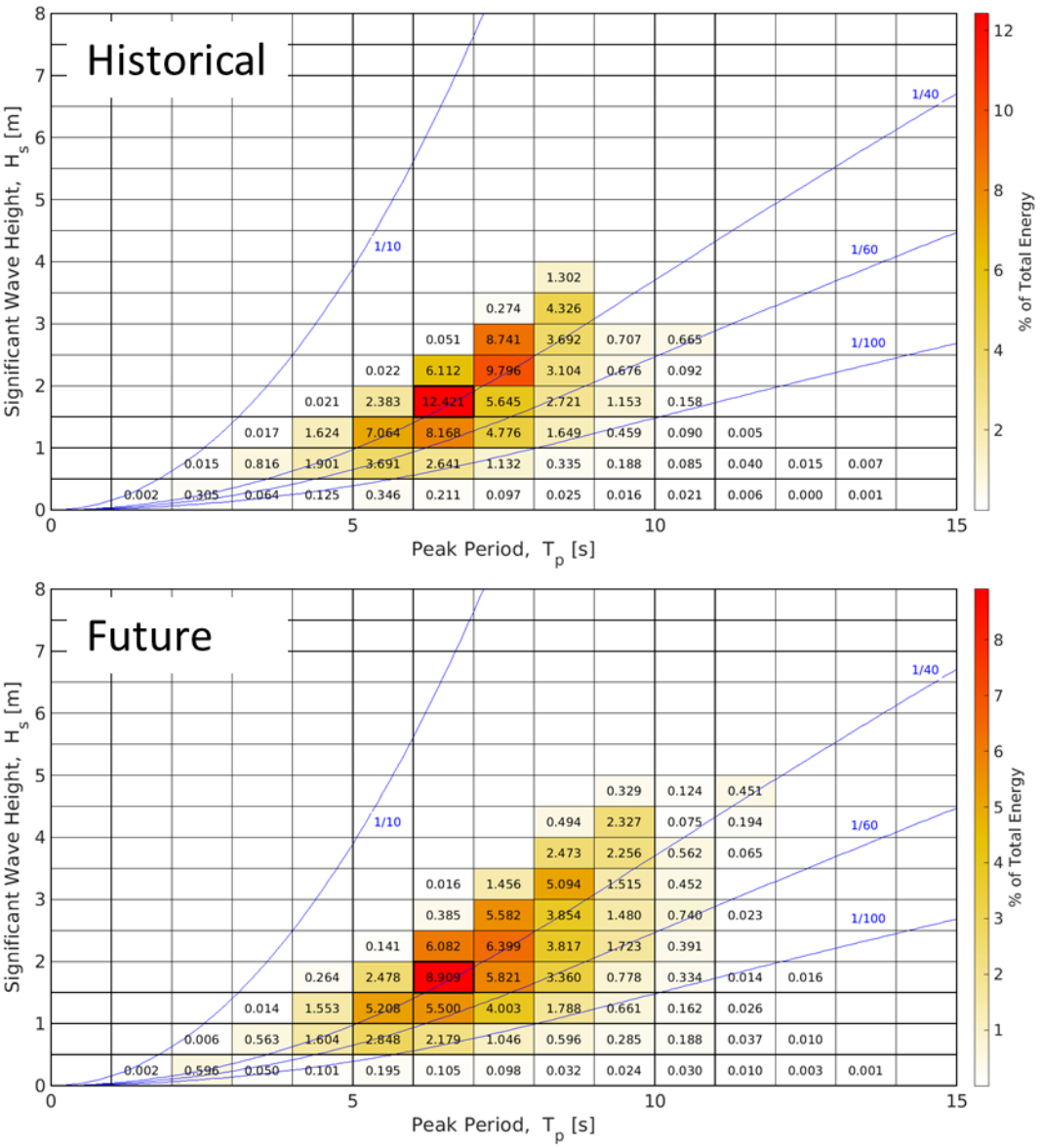

Figure 3. Energy-weighted occurrence JPD at the Site 4 for (top) Historical (2007-2019) and (bottom) Future (2020-2040) time periods. Blue lines indicate constant steepness curves (steepness^{-1} = λ_{Tp}/H_s, where λ_{Tp} is the wavelength of the peak period). Energy-weighted occurrence is represented both numerically and through color and is used to determine the contribution from each cluster to the AAP flux.

3. Methods to Develop Typologies

3.1. K-Means Clustering Analysis

Previous work has established k-means clustering of the JPD of H_s and T_p as a useful quantization technique to assess oceanographic data (Bull and Dallman, 2017; Camus et al., 2011) and we have extended the process to a new study area encompassing six sites across the North Slope of Alaska (Figure 1). K-means clustering was applied to the energy-weighted JPD of significant wave height (H_s) and peak period (T_p). from each site to identify Location-Dependent cluster centroids for six sea states. Location-Independent centroids were determined through an averaging procedure of the Location-Dependent centroids; subsequent membership to the Location-Independent centroids was then found for each site. Incorporating the associated Location-Dependent wave direction, salinity, temperature, and wind data allows for the complete definition of oceanographic boundary conditions (i.e., the typology) to be used in nearshore models. Location-dependence for each site is established through the occurrence JPD in the form of unique scaling factors representing the fraction of time that the typology would occupy over a representative year. Both the Historical and Future data sets are clustered independently as stationarity in the face of future climate change conditions is not expected.

Our k-means analysis occurs in three Phases for both the Historical and Future timespans. In Phase 1, we apply the built-in *kmeans.m* function of MATLAB on the energy-weighted occurrence of H_s and T_p at each site in order to choose k different but prototypical representations of the energy-weighted occurrence diagram that minimizes within cluster variances. To initialize the k-means process, a set of k pairs of H_s-T_p values are selected uniformly at random from the full set of energy-weighted occurrence JPD values at a given site. The squared Euclidean distances, SED_{ik}, between these k pairs and the pairs from each sample i in the JPD are calculated as:

$$SED_{ik} = \sqrt[2]{(H_{si} - H_{sk})^2 + (T_{pi} - T_{pk})^2} \qquad \text{(Equation 4)},$$

where H_{sk} and T_{pk} are the centroid values for significant wave height and peak period for the k^{th} cluster and H_{si} and T_{pi} are the significant wave height and peak period values for the i^{th} point in the JPD for a specific site. In this way, each point in the JPD is compared to each cluster centroid and then assigned as a member of the centroid for which this distance, SED_{ik}, is minimized. After the distances and assignments are determined, updated centroid clusters (H_{sk} and T_{pk}) are recalculated by taking the average H_s and T_p values from all members of each cluster and the distance and

assignment calculations are repeated. The total squared Euclidean distance, SED_K, is the objective function of the algorithm determined as the sum of all K of the individual cluster distances for only their respective members:

$$SED_K = \sum_1^K \min SED_{ik} \quad \text{(Equation 5)},$$

where the minimum SED_{ik} is used to assign sample i to cluster k. The k-means clustering process continues until SED_K no longer decreases when the new centroids are calculated. To determine the minimum solution for the objective function, the algorithm is run for 100 iterations with a different set of randomly selected starting H_s-T_p centroids each time. The final outputs of the algorithm are the H_s and T_p values for each centroid cluster, as well as the identification number (1 through k) that is used to assign each pair as a member of the centroid with the lowest squared Euclidean distance. This preliminary set of data is referred to as the Location-Dependent cluster results.

The goal of Phase 2 is to identify a single set of cluster centroids that best represents the ocean conditions across the North Slope of Alaska. Because each site contains unique geophysical data and will therefore produce variable centroids for the six target sea states, we collect all of the Location-Dependent centroids and calculate six average centroid values. The individual centroids are sorted by increasing T_p value and then averaged together to calculate the preliminary centroid pool for the six Location-Independent clusters.

These average values are then adjusted according to the following three principles: 1)The sea states should represent distinct peak periods and no single sea state should be dominant (i.e., not exceed 40%) with respect the contribution to AAP flux (Bull and Dallman, 2017). Summing the energy-weighted occurrence from all centroid members results in the weighted power flux for that centroid to the AAP flux at that site. The contribution of each centroid to the AAP (C_k) is simply the ratio of the weighted power flux for that centroid to the total AAP flux; 2) We additionally seek clusters that plot along lines of constant inverse steepness, a ratio of the wavelength based on T_p (λ_{Tp}) and water depth to H_s. As informed by Location-Dependent centroids, these target inverse steepness values (with increasing T_p value) are 35-40-60-40-60-50 for the Historical data, and for the Future data they are 35-40-50-45-50-40. The average T_p values are rounded and the H_s is adjusted until the centroid lies upon the targeted constant steepness curve. Outputs from Phase 2 identify the Location-Independent centroid values.

Once the Location-Independent centroids are determined, we then calculate membership to those centroids for each location. In this final clustering step (Phase 3), each location's H_s-T_p

pair is reclassified using the values of SED_{ik} based on the distance from the Location-Independent centroids calculated in Phase 2 to establish the final cluster memberships for each centroid. Since the centroids do not represent the minimum distance calculation, the Phase 3 SED_K calculation for each site will yield a higher value than those from the Location-Dependent clustering conducted in Phase 1. Because the data sets and target inverse steepness values differ between the Historical and Future timespans, the clustering routine will yield different results for each sea state at the same sites in the two timespans.

3.2. Distribution Evaluation

Although the clustering routine only uses the H_s and T_p datasets, the memberships of the Location-Dependent H_s and T_p pairs are temporally associated with additional oceanographic and atmospheric data needed to establish the boundary conditions for nearshore modeling. For each Location-Independent centroid, the distributions of wave direction, water level, wind speed, and wind direction at each site are evaluated to determine a representative value for each parameter. Selection of the representative values for each cluster is a flexible process that is based upon diverse climate and oceanographic considerations. The technique was used by Bull and Dallman (2017) and is most advantageous when the underlying wave, water, and wind data have a large spread as seen in the six sites across the North Slope. We seek diversity in clusters based on combinations of the directionality (i.e., we want wave and wind influences from different directions), wind speed (i.e., we want clusters that span both high and low energy ocean conditions), and water level (i.e., we want clusters associated with storm events to have elevated water level and clusters associated with calm conditions to have decreased water level). The guidelines that we established for our selection process are described in the next section.

In order to generalize the effects of the sea states on nearshore processes with shorelines of variable orientation, the wave and wind orientations were modified with respect to the coastline geometry to normalize the variability. For each site in the study area, we determined the shoreline orientation at the nearest onshore location. The wave and wind orientations from every site were rotated by the angle perpendicular to the shoreline so that the coastline runs along a horizontal direction in map view (Figure 4). The rotated wave and wind data at each site are then evaluated to assess the distributions across the full study area.

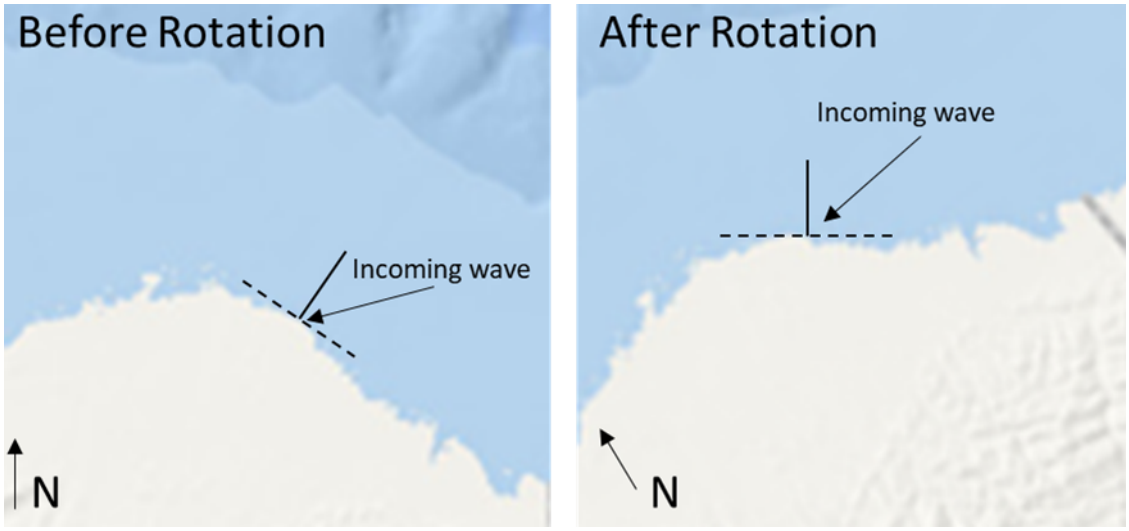

Figure 4. Example coastline rotation with shoreline orientation shown as dashed line and perpendicular orientation shown as solid line. For an incoming wave [or wind] direction (arrow), the orientation is rotated such that the shoreline orientation runs 180°-90° and the associated change in the North direction is shown by the black arrow on the bottom left.

Normalized distributions of each associated parameter were plotted for all sites and we determined a single value for the wave direction, wind direction, wind speed, and water level based nominally on the modal peak of these distributions. We define the modal peak as the parameter value with the highest normalized value based on distribution profiles at the six analysis sites. In the simplest terms, a unimodal distribution indicates a clear influence of the geophysical data on the selected parameter value. However due to variability in most distributions, multiple representative values can be associated with each sea state and we determine both a preferred and alternative value when the distributions are more complicated. While our primary cluster selections will be synchronized with respect to wave and water direction, we are also interested in the effects of more complex sea states where the wave and wind directions may be sourced from opposing directions. These alternatives again reflect the considerations regarding our target diversity goals and can be used as inputs for simulations to assess differences in resulting nearshore conditions.

3.3. Guidelines for Final Typology Selection

In order to describe boundary conditions that encompass the entire offshore environment for the Historical and Future timespans, we developed a set of guidelines in our selection process:

a.) *Consistent wave and wind cardinal directions*: because the wind and wave energies tend to be related, the directions of these sea state values will be generally similar, but not identical and thus in our selection process, we define similarity as stemming from the same

quadrant (i.e., N-E or N-W). Alternative selections will allow for mixing of the wave and wind directions in sea states where the $T_p > 8$ s indicating distantly generated swell as a way to evaluate the effects of more complicated environmental behavior.

b.) *Wind directions influence water level*: water level will be raised by Ekman transport if wind energy comes from the west and lowered if wind energy comes from the east (Barnhart et al., 2014b; Griffiths et al., 1983; Hachmeister, 1985; Reimnitz and Maurer, 1979; Weingartner et al., 2017).

c.) *A majority of the AAP flux should come from the east*: local and regional studies of past and future conditions indicate that storm tracks and incident deep water waves primarily come from the north to east quadrant and somewhat less frequently from the west to north quadrant (Erikson et al., 2020; Hamilton et al., 2021). The selection process reflects this in that the contribution of sea states with N-N or E-E wave-wind directions need to contribute on average >50% of the AAP flux for each of the six sites.

d.) *Ensure representation of westerly storm clusters*: whereas both easterly and westerly Arctic storm tracks contribute to the AAP, winds from the west raise water levels at the coast through Ekman transport (Coriolis force deflecting water to the right in the northern hemisphere) enabling waves to act higher on the shore profile (Barnhart et al., 2014b; Erikson et al., 2020; Pond and Pickard, 1983). In contrast, easterly storms cause currents to move toward the west, deflect to the right, and offshore yielding a setdown and drawdown of water from the coast. W-W wave-wind orientations are thus prioritized in the final typological selection to capture the greater potential for erosion-driving events.

3.4. Salinity and Temperature

The time series for temperature and salinity showed less variation at all sites in the study area than the distribution data (e.g., H_s, T_p, D_e, etc.), hence we determined the average profiles for all sites using Historical data. For salinity, we collected GOFS 3.1 data for the six sites between 2008-2015 and determined the average profile from July 1 to November 28 at each site. We then calculated a representative salinity profile by taking the mean of these six average profiles. From this representative profile, we calculated the ice-free season average (μ_s) and standard deviation (σ_s) for the Arctic Ocean salinity. The Historical salinity value was then set to μ_s and because salinity data were unavailable for the Future timespan, the Future value was set to $\mu_s - \sigma_s$, reflecting the expected decrease in salinity as Arctic ice melts in the future.

We repeated this process for temperature where we collected the ASRv2 skin temperature data at the nearest location to each site for the years 2007-2016 and calculated average profiles. Again, we took the mean of these average profiles to construct the representative temperature profile for the Arctic Ocean. To select a single temperature value for both timespans, we calculated the average temperature (μ_T) and standard deviation (σ_T) from a 72-hour window in late summer (August 27-29) and set the Historical value to μ_T. Although sea surface temperatures are available for GFDL-CM3, the SNAP downscaling process was not optimized to account for sea surface temperatures. Thus, similar to salinity, Future values were simplistically set to $\mu_T + \sigma_T$ to reflect the expected increase in Arctic temperatures during 2020-2040.

3.5. Translating between location independence and location dependence

Our final selections for each of the sea states in the Historical and Future timespans include the H_s and T_p values calculated using k-means clustering and the associated values for wave direction, water level, wind direction, wind speed, temperature, and salinity. The goal of this process is to calculate and determine boundary conditions that are prototypical for the entire North Slope for both Historical and Future timespans to minimize required computational intensity. However, these Location-Independent oceanographic conditions that will be experienced across the entire study area require apportionment in a Location-Dependent manner at each site during the ice-free season.

Location-Dependence can be reintroduced by determining the statistical probability of the Location-Independent centroid occurring at the specific site (i.e., representing the fraction of time that the centroid would occupy over a representative year). To achieve this goal, the occurrence values in the occurrence JPD associated with the Location-Independent centroids are summed (Figure 3). These data served as the basis for site-specific time apportionment component of the typologies presented in the next section.

4. Typological Results

4.1 Location-Dependent versus Location-Independent H_s-T_p Clusters

Following the methods described in Section 3.1, each site was analyzed to determine the Location-Dependent and Location-Independent centroids. A graphical example of the k-means clustering membership (colors) and centroids (×'s) for Site 4 is shown in Figure 5 (remaining sites shown in Appendix Figures A11 – A15); the top row shows the Historical Location-Dependent

and Location-Independent clusters, while the bottom row shows the Future Location-Dependent and Location-Independent clusters.

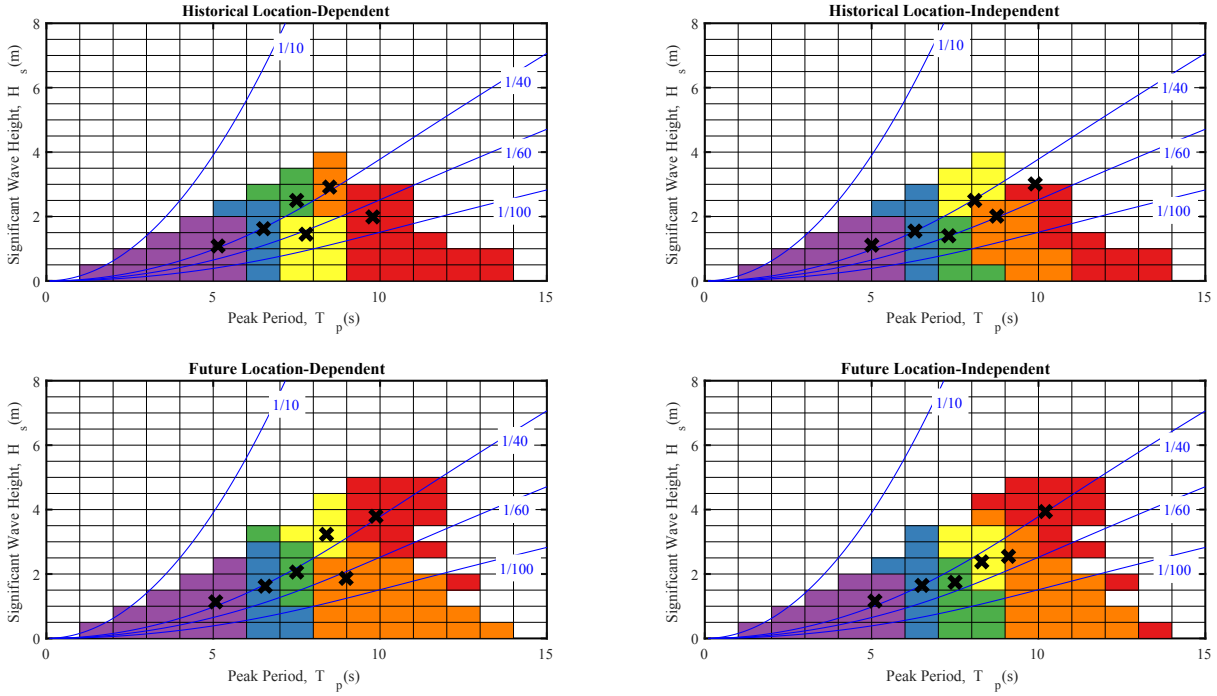

Figure 5. Color coded clusters showing the H_s and T_p bins associated with each cluster at Site 4. Cluster centroids are indicated by the black × in each group. Note that the membership of each H_s-T_p bin can change between Historical and Future time spans as well as when clustered using Location-Dependent or Location-Independent centroids. Compare the bins to those associated with the intensities for the Occurrence and Energy Weighted Occurrence in Figures 2 and 3.

Tabular data summarizing the Location-Dependent and the Location-Independent centroids for all sites are shown for the Historical timespan in Table 1 and the Future timespan in Table 2. Because the Location-Independent centroids do not represent a minimum solution for the k-means algorithm, the values of SED_K increase between the Location-Dependent and Location-Independent clusters at all sites for both timespans. By definition, the site-specific AAP flux values remain consistent between both clustering styles but increase between the Historical and Future timespan due to the higher overall energy in the study area in the future. The Location-Dependent and Location-Independent weighted power flux and contribution to total AAP (C_k) values in Tables 1 and 2 show how each cluster's centroid uniquely contributes to differing sites as well as between the Historical and Future timespans.

Table 1. Details for Historical centroids for Location-Dependent (left) and Location-Independent (right) analysis. Minor differences in Location-Independent Steepness^{-1} values result from small variations in depth at each site. SED_K values are taken as the sum of all minimum squared Euclidean distances for all members of each cluster. AAP flux is equal to the sum of the members for each centroid of the Weighted Power Flux at each site and will be identical between Location-Dependent and Location-Independent analyses.

	Location Dependent					Location Independent				
Site 1	**Tp (s)**	**Hs (m)**	**Steepness^{-1} (λ_{Tp}/Hs)**	**Weighted Power Flux (kW/m)**	**C_k**	**Tp (s)**	**Hs (m)**	**Steepness^{-1} (λ_{Tp}/Hs)**	**Weighted Power Flux (kW/m)**	**C_k**
Cluster 1	5.25	1.23	35	1.43	12.6%	5.00	1.11	35	1.42	12.5%
Cluster 2	6.52	1.73	38	2.49	21.8%	6.30	1.55	40	2.45	21.5%
Cluster 3	7.50	2.21	40	2.87	25.2%	7.30	1.40	59	0.85	7.5%
Cluster 4	8.44	3.17	35	1.81	15.9%	8.10	2.50	41	3.87	34.0%
Cluster 5	8.89	2.09	58	1.33	11.7%	8.75	2.00	59	1.11	9.8%
Cluster 6	9.69	3.90	37	1.45	12.7%	9.90	3.00	49	1.67	14.7%
	SED_K : 1432323		AAP:	11.38		SED_K : 2561456		AAP:	11.38	
Site 2	**Tp (s)**	**Hs (m)**	**Steepness^{-1} (λ_{Tp}/Hs)**	**Weighted Power Flux (kW/m)**	**C_k**	**Tp (s)**	**Hs (m)**	**Steepness^{-1} (λ_{Tp}/Hs)**	**Weighted Power Flux (kW/m)**	**C_k**
Cluster 1	5.24	1.21	35	1.36	13.7%	5.00	1.11	35	1.35	13.7%
Cluster 2	6.50	1.76	38	2.47	25.0%	6.30	1.55	40	2.48	25.0%
Cluster 3	7.50	2.12	41	2.38	24.1%	7.30	1.40	59	0.86	8.7%
Cluster 4	8.43	3.10	35	1.47	14.8%	8.10	2.50	40	2.99	30.3%
Cluster 5	8.82	2.06	58	1.26	12.7%	8.75	2.00	58	1.10	11.1%
Cluster 6	9.77	3.77	37	0.94	9.6%	9.90	3.00	48	1.11	11.2%
	SED_K : 1471306		AAP:	9.89		SED_K : 2233107		AAP:	9.89	
Site 3	**Tp (s)**	**Hs (m)**	**Steepness^{-1} (λ_{Tp}/Hs)**	**Weighted Power Flux (kW/m)**	**C_k**	**Tp (s)**	**Hs (m)**	**Steepness^{-1} (λ_{Tp}/Hs)**	**Weighted Power Flux (kW/m)**	**C_k**
Cluster 1	5.10	1.04	39	0.84	15.3%	5.00	1.11	35	0.84	15.3%
Cluster 2	6.50	1.48	45	1.30	23.6%	6.30	1.55	40	1.30	23.6%
Cluster 3	7.50	1.72	51	1.24	22.6%	7.30	1.40	59	0.82	15.0%
Cluster 4	8.35	2.66	40	0.92	16.7%	8.10	2.50	41	1.03	18.7%
Cluster 5	8.77	1.54	76	0.66	12.1%	8.75	2.00	59	1.11	20.3%
Cluster 6	9.94	2.80	53	0.53	9.7%	9.90	3.00	49	0.39	7.0%
	SED_K : 1717403		AAP:	5.50		SED_K : 1981135		AAP:	5.50	
Site 4	**Tp (s)**	**Hs (m)**	**Steepness^{-1} (λ_{Tp}/Hs)**	**Weighted Power Flux (kW/m)**	**C_k**	**Tp (s)**	**Hs (m)**	**Steepness^{-1} (λ_{Tp}/Hs)**	**Weighted Power Flux (kW/m)**	**C_k**
Cluster 1	5.15	1.09	38	1.01	18.4%	5.00	1.11	35	1.01	18.4%
Cluster 2	6.50	1.62	41	1.62	29.6%	6.30	1.55	40	1.62	29.6%
Cluster 3	7.50	2.50	35	1.03	18.9%	7.30	1.40	59	0.64	11.7%
Cluster 4	7.79	1.45	65	0.90	16.4%	8.10	2.50	41	1.54	28.1%
Cluster 5	8.50	2.90	38	0.68	12.4%	8.75	2.00	59	0.57	10.4%
Cluster 6	9.79	2.00	72	0.24	4.4%	9.90	3.00	49	0.10	1.8%
	SED_K : 1397613		AAP:	5.47		SED_K : 1981693		AAP:	5.47	
Site 5	**Tp (s)**	**Hs (m)**	**Steepness^{-1} (λ_{Tp}/Hs)**	**Weighted Power Flux (kW/m)**	**C_k**	**Tp (s)**	**Hs (m)**	**Steepness^{-1} (λ_{Tp}/Hs)**	**Weighted Power Flux (kW/m)**	**C_k**
Cluster 1	5.15	1.18	35	1.23	20.2%	5.00	1.11	35	1.22	20.1%
Cluster 2	6.50	1.68	39	1.59	26.2%	6.30	1.55	40	1.63	26.7%
Cluster 3	7.48	2.61	33	1.11	18.3%	7.30	1.40	59	0.58	9.6%
Cluster 4	7.85	1.45	66	0.86	14.1%	8.10	2.50	41	1.94	31.8%
Cluster 5	8.58	2.82	40	0.93	15.3%	8.75	2.00	59	0.50	8.3%
Cluster 6	9.06	4.10	31	0.36	6.0%	9.90	3.00	49	0.21	3.5%
	SED_K : 1589578		AAP:	6.08		SED_K : 2493141		AAP:	6.08	
Site 6	**Tp (s)**	**Hs (m)**	**Steepness^{-1} (λ_{Tp}/Hs)**	**Weighted Power Flux (kW/m)**	**C_k**	**Tp (s)**	**Hs (m)**	**Steepness^{-1} (λ_{Tp}/Hs)**	**Weighted Power Flux (kW/m)**	**C_k**
Cluster 1	4.19	0.91	30	0.50	12.7%	5.00	1.11	35	1.32	33.9%
Cluster 2	5.50	1.29	37	0.83	21.3%	6.30	1.55	40	1.02	26.3%
Cluster 3	6.50	1.67	40	1.02	26.2%	7.30	1.40	59	0.39	9.9%
Cluster 4	7.85	1.41	68	0.59	15.2%	8.10	2.50	41	0.59	15.2%
Cluster 5	7.87	2.57	37	0.67	17.3%	8.75	2.00	59	0.45	11.6%
Cluster 6	9.83	2.09	70	0.29	7.4%	9.90	3.00	49	0.12	3.0%
	SED_K : 1619455		AAP:	3.90		SED_K : 2442970		AAP:	3.90	

Table 2. Details for Future centroids for Location-Dependent (left) and Location-Independent (right) analysis. Minor differences in Location-Independent Steepness^{-1} values result from small variations in depth at each site. SED_K values are taken as the sum of all minimum squared Euclidean distances for all members of each cluster. AAP flux is equal to the sum of the members for each centroid of the Weighted Power Flux at each site and will be identical between Location-Dependent and Location-Independent analyses.

	Location Dependent					Location Independent				
Site 1	**Tp (s)**	**Hs (m)**	**Steepness^{-1} (λ_{Tp}/Hs)**	**Weighted Power Flux (kW/m)**	**C_k**	**Tp (s)**	**Hs (m)**	**Steepness^{-1} (λ_{Tp}/Hs)**	**Weighted Power Flux (kW/m)**	**C_k**
Cluster 1	5.24	1.16	37	0.99	7.7%	5.10	1.15	35	0.98	7.7%
Cluster 2	6.97	1.82	42	3.45	26.9%	6.50	1.65	40	1.84	14.3%
Cluster 3	8.18	3.10	34	3.10	24.1%	7.50	1.75	50	1.75	13.6%
Cluster 4	9.01	2.09	60	1.60	12.5%	8.30	2.37	45	3.36	26.1%
Cluster 5	9.78	3.86	38	2.43	18.9%	9.10	2.55	50	1.55	12.1%
Cluster 6	11.09	5.39	33	1.26	9.8%	10.20	3.95	40	3.36	26.2%
	SED_K : 5214539		AAP:	12.84		SED_K : 8908766		AAP:	12.84	
Site 2	**Tp (s)**	**Hs (m)**	**Steepness^{-1} (λ_{Tp}/Hs)**	**Weighted Power Flux (kW/m)**	**C_k**	**Tp (s)**	**Hs (m)**	**Steepness^{-1} (λ_{Tp}/Hs)**	**Weighted Power Flux (kW/m)**	**C_k**
Cluster 1	5.22	1.19	36	1.09	9.7%	5.10	1.15	35	1.08	9.6%
Cluster 2	6.95	1.84	41	3.36	29.9%	6.50	1.65	40	1.87	16.6%
Cluster 3	8.15	3.07	33	2.47	22.0%	7.50	1.75	50	1.63	14.5%
Cluster 4	8.88	1.91	63	1.26	11.2%	8.30	2.37	45	2.86	25.4%
Cluster 5	9.69	3.59	39	2.08	18.5%	9.10	2.55	49	1.42	12.6%
Cluster 6	10.94	5.07	33	0.99	8.8%	10.20	3.95	38	2.39	21.3%
	SED_K : 5094423		AAP:	11.25		SED_K : 7436083		AAP:	11.25	
Site 3	**Tp (s)**	**Hs (m)**	**Steepness^{-1} (λ_{Tp}/Hs)**	**Weighted Power Flux (kW/m)**	**C_k**	**Tp (s)**	**Hs (m)**	**Steepness^{-1} (λ_{Tp}/Hs)**	**Weighted Power Flux (kW/m)**	**C_k**
Cluster 1	5.08	1.05	38	0.69	11.5%	5.10	1.15	35	0.69	11.5%
Cluster 2	6.50	1.54	43	1.04	17.5%	6.50	1.65	40	1.04	17.5%
Cluster 3	7.78	1.68	56	1.71	28.8%	7.50	1.75	50	1.39	23.5%
Cluster 4	8.35	2.76	39	1.16	19.5%	8.30	2.37	45	1.43	24.1%
Cluster 5	9.81	2.07	69	0.64	10.8%	9.10	2.55	49	0.85	14.3%
Cluster 6	9.87	3.73	39	0.71	11.9%	10.20	3.95	39	0.54	9.2%
	SED_K : 4631461		AAP:	5.93		SED_K : 5716827		AAP:	5.93	
Site 4	**Tp (s)**	**Hs (m)**	**Steepness^{-1} (λ_{Tp}/Hs)**	**Weighted Power Flux (kW/m)**	**C_k**	**Tp (s)**	**Hs (m)**	**Steepness^{-1} (λ_{Tp}/Hs)**	**Weighted Power Flux (kW/m)**	**C_k**
Cluster 1	5.08	1.13	36	0.87	15.6%	5.10	1.15	35	0.86	15.5%
Cluster 2	6.55	1.63	41	1.35	24.3%	6.50	1.65	40	1.29	23.3%
Cluster 3	7.50	2.06	42	1.21	21.8%	7.50	1.75	50	1.10	19.8%
Cluster 4	8.39	3.24	34	0.74	13.4%	8.30	2.37	45	1.28	23.2%
Cluster 5	8.97	1.87	66	0.87	15.7%	9.10	2.55	49	0.56	10.1%
Cluster 6	9.88	3.80	38	0.51	9.1%	10.20	3.95	39	0.45	8.1%
	SED_K : 4851356		AAP:	5.54		SED_K : 6079083		AAP:	5.54	
Site 5	**Tp (s)**	**Hs (m)**	**Steepness^{-1} (λ_{Tp}/Hs)**	**Weighted Power Flux (kW/m)**	**C_k**	**Tp (s)**	**Hs (m)**	**Steepness^{-1} (λ_{Tp}/Hs)**	**Weighted Power Flux (kW/m)**	**C_k**
Cluster 1	4.12	0.87	30	0.30	5.9%	5.10	1.15	35	1.00	19.5%
Cluster 2	5.50	1.28	37	0.70	13.7%	6.50	1.65	40	1.25	24.5%
Cluster 3	6.50	1.69	39	1.24	24.3%	7.50	1.75	50	1.03	20.2%
Cluster 4	7.88	1.76	55	1.44	28.2%	8.30	2.37	45	1.14	22.4%
Cluster 5	8.07	3.16	32	0.99	19.4%	9.10	2.55	50	0.43	8.4%
Cluster 6	9.89	3.08	48	0.43	8.4%	10.20	3.95	39	0.26	5.0%
	SED_K : 4783572		AAP:	5.10		SED_K : 6096079		AAP:	5.10	
Site 6	**Tp (s)**	**Hs (m)**	**Steepness^{-1} (λ_{Tp}/Hs)**	**Weighted Power Flux (kW/m)**	**C_k**	**Tp (s)**	**Hs (m)**	**Steepness^{-1} (λ_{Tp}/Hs)**	**Weighted Power Flux (kW/m)**	**C_k**
Cluster 1	4.14	0.87	31	0.41	9.5%	5.10	1.15	35	1.07	25.1%
Cluster 2	5.51	1.27	37	0.67	15.7%	6.50	1.65	40	1.12	26.4%
Cluster 3	6.50	1.68	39	1.11	26.2%	7.50	1.75	50	0.79	18.6%
Cluster 4	7.72	1.71	54	0.89	20.9%	8.30	2.37	45	0.79	18.6%
Cluster 5	8.20	2.82	37	0.73	17.2%	9.10	2.55	50	0.32	7.6%
Cluster 6	9.99	2.64	57	0.44	10.5%	10.20	3.95	39	0.16	3.8%
	SED_K : 4591875		AAP:	4.25		SED_K : 6174976		AAP:	4.25	

The centroid pairs of Location-Independent H_s and T_p for the Historical and Future timespans show how these parameters are expected to change over the next two decades years (Figure 6). All values of H_s and T_p increase for each centroid between the Historical and Future timespans except for centroid 4 where the H_s value drops from 2.50 m to 2.37 m. These elevated H_s and T_p values in the Future reflect an increase in energy likely associated with longer duration and greater areal ice-free ocean conditions generating increased fetch (Casas-Prat and Wang, 2020b; Thomson et al., 2016).

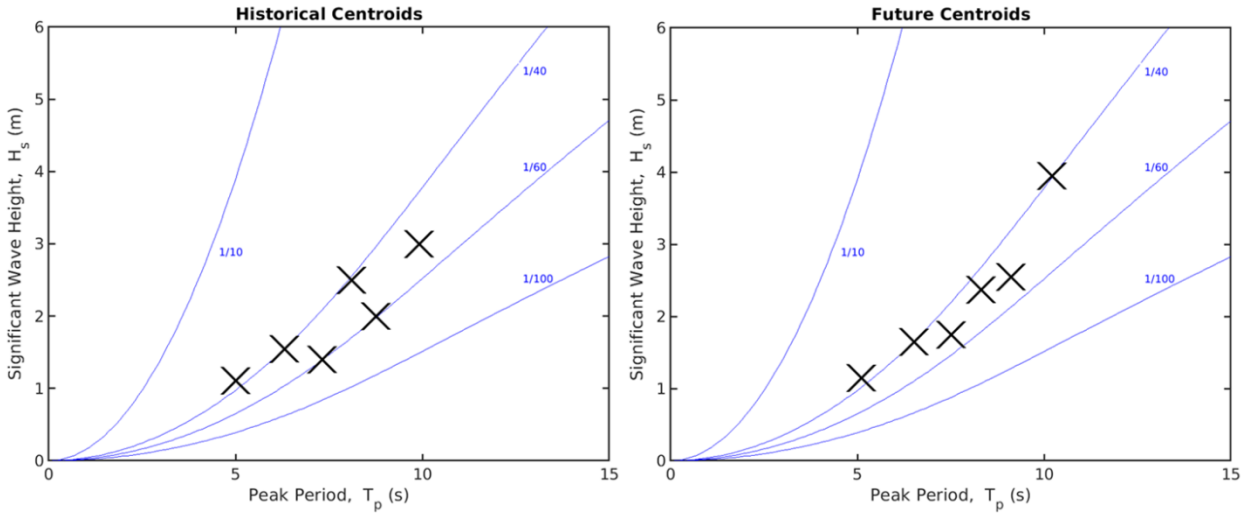

Figure 6. Location-Independent centroids (×'s) for the Historical (left) and Future (right) timespans. The centroid inverse steepness targets (in order of increasing T_p value) change from 35-40-60-40-60-50 during the Historical timespan to 35-40-50-45-50-40 for the Future timespan.

4.2 Distribution Analysis

Following the guidelines established in Section 3.3, we determined the normalized distributions for wave direction, wind direction, wind speed, and water level at all sites for the Historical (Figure 7) and Future (Figure 8) timespans. For each cluster, associated parameter values were subjectively chosen based on their distributions from all sites (Tables 3 and 4). Alternative values for each parameter were also selected for most clusters when the distributions allowed and are provided in the Appendix (Tables A2 and A3).

The orientations for the wave and wind directions were consistent between the two timespans so that Clusters 1, 2, and 4 were sourced from the east (between 24° to 113°) and

Clusters 3, 5, and 6 were sourced from the west (between 250° to 342°). Based on the contributions to the AAP flux calculated for all stations, the easterly clusters (1, 2, and 4) account for 70.8% of the AAP flux during the Historical timespan and 58.5% in the Future timespan, with the remaining contributions coming from the westerly clusters (3, 5, and 6). Our guideline that eastern sea states account for >50% of the AAP flux was met for both timespans and the reduction in eastern contributions in the Future follows our expectation that more energy will be sourced from the west.

The water levels associated with each cluster ranged from -0.20 m to +0.30 m, and the direction (positive (surge) or negative (setdown)) determined by the orientation of the source wave and wind data. Distributions in the water level for Clusters 1 and 2 in the Future timespan suggested that these clusters should exhibit positive values, however to enforce the guideline presented in Section 3.3 that east-sourced clusters will lower the water level (Barnhart et al., 2014b), we chose to force these clusters to have water levels with negative, but moderate, magnitudes. Generally, the magnitude of the water level was dictated by the wind speed, with the maximum wind speed corresponding to the highest magnitude in both the Historical and Future timespans; however, the correlation between positive and negative water levels is only strong when wind speeds exceed ~12 m/s (Erikson et al., 2020; Joyce et al., 2019; Lynch et al., 2008). The wind speeds ranged from 4.9 to 13.0 m/s in the Historical timespan and 5.0 to 16.0 m/s in the Future, with Clusters 4 and 6 representing the highest speeds from the east and west orientations, respectively. Cluster 6 also represents the highest storm cluster in both timespans and accordingly has the highest water level surge, which increases in magnitude for the Future data set as we expect Arctic storm events to strengthen in response to climate change (Casas-Prat and Wang, 2020a; Day and Hodges, 2018; Erikson et al., 2016; Manson and Solomon, 2007). All clusters maintained or increased wind speed in the Future except for Cluster 5 which decreased from 7.5 to 5.0 m/s.

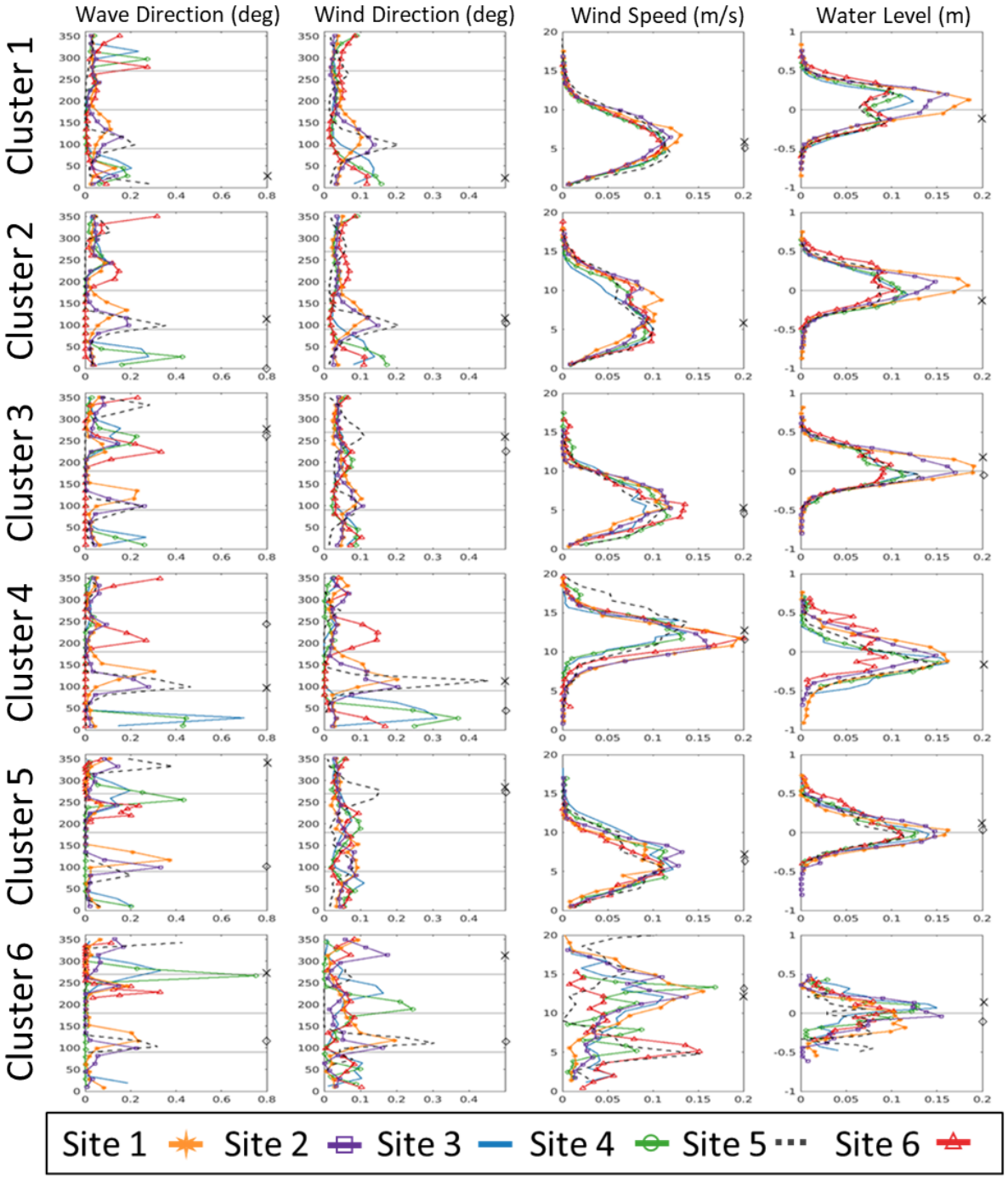

Figure 7. Historical clustering distribution results for all sites. The normalized distributions for wave direction (first column), wind direction (second column), wind speed (third column), and water level (fourth column) are shown for each cluster. Site profiles are identified by line style and color throughout the plots. Preferred values are indicated with × while alternative selections are indicated with a diamond; note, not all clusters have alternative selections.

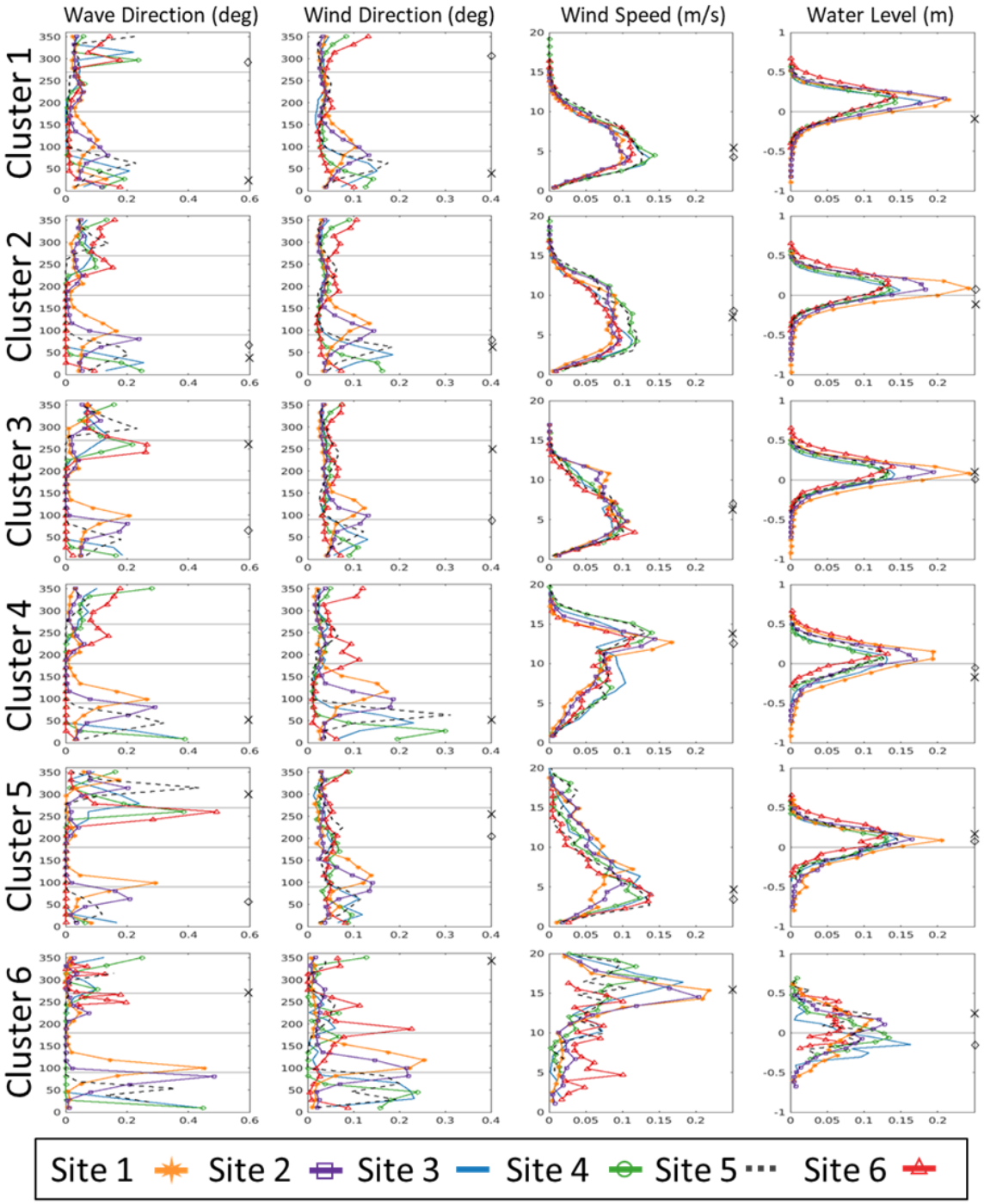

Figure 8. Future clustering distribution results for all sites. The normalized distributions for wave direction (first column), wind direction (second column), wind speed (third column), and water level (fourth column) are shown for each cluster. Site profiles are identified by line style and color throughout the plots. Selected values are indicated with × while alternative selections are indicated with a diamond; not all clusters have an alternative option; note, not all clusters have alternative selections.

4.3 Salinity and Temperature

The methods described in Section 3.3 yielded an average annual timeseries for temperature and salinity based on the Historical data from all six sites (Figure 9). The average temperature at all sites associated with the 72-hour period between August 27-29 of each year produced a μ_T of 3.68°C and a standard deviation (σ_T) of 1.34°C. The Historical value was set to 3.68°C while the Future value increased to 5.02°C.

For salinity, the average values during the ice-free season at each site provided a μ_S of 29.60 psu and a σ_S of 0.71 psu. This resulted in setting the salinity to 29.60 psu for the Historical timespan and 28.89 psu for the Future. The selections for both parameters represent constant values over the two timespans for all six clusters. The increase in temperature and decrease in salinity associated with the Future values is a proxy for expected ice melt in the Arctic.

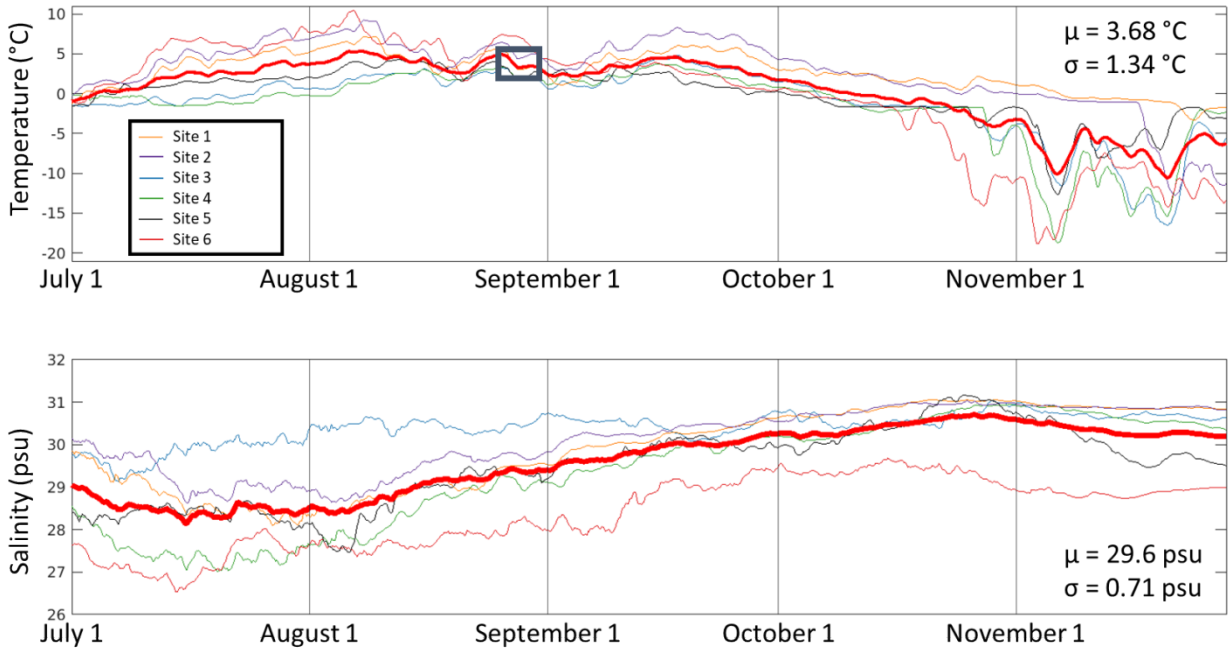

Figure 9. Historical average temperature (top) and salinity (bottom) profiles for each site are shown by thin lines with average profile based on all sites shown as thick red line. Single temperature value is based on the average temperatures between August 27-29 (gray box) and single salinity value is based on average of the full ice-free season.

4.4 Typological Representation of the Offshore North Slope Oceanographic Environment

The final six typologies for the Historical and Future data sets represent the best approximation of the six sets of conditions that will encompass the oceanographic environment

along the North Slope of Alaska during these respective timespans. These typologies are shown in Tables 3 and 4. Constant salinity and temperature values identified in Section 4.3 are associated with these typologies.

Table 3. Final Historical typology. Each parameter is Location-Independent and general for each of the six sites.

Historic	Tp (s)	Hs (m)	Wave Direction	Water Level (m)	Wind Direction	Wind Speed (m/s)	Wave-Wind Orientation
Cluster 1	5.00	1.11	33	-0.15	29	5.5	N-N
Cluster 2	6.30	1.55	113	-0.10	113	6.0	E-E
Cluster 3	7.30	1.40	270	+0.15	263	4.9	W-W
Cluster 4	8.10	2.50	98	-0.20	113	13.0	E-E
Cluster 5	8.75	2.00	330	+0.10	280	7.5	W-W
Cluster 6	9.90	3.00	280	+0.20	316	12.0	W-W

Table 4. Final Future typology. Each parameter is Location-Independent and general for each of the six sites. Asterisks on water levels for Clusters 1 and 2 indicate they were forced based on guidelines in Section 3.3 instead of purely from the data distributions.

Future	Tp (s)	Hs (m)	Wave Direction	Water Level (m)	Wind Direction	Wind Speed (m/s)	Wave-Wind Orientation
Cluster 1	5.10	1.15	24	-0.05*	40	5.5	N-N
Cluster 2	6.50	1.65	45	-0.10*	69	7.5	E-E
Cluster 3	7.50	1.75	270	+0.15	250	6.5	W-W
Cluster 4	8.30	2.37	61	-0.20	53	14.0	E-E
Cluster 5	9.10	2.55	313	+0.10	260	5.0	W-W
Cluster 6	10.20	3.95	280	+0.30	342	16.0	W-W

As discussed in Section 3.5, it is possible to apportion the Location-Independent typological conditions in a Location-Dependent manner at each site during the ice-free season through summation of the occurrence JPD values for each cluster centroid. Table 5 identifies the fraction of time that the centroid would occupy over a representative year for Historical and Future conditions based on the occurrences of H_s-T_p for each cluster and each site. In a similar way to the contributions to AAP flux, the apportionment results identify changes between clusters from different source directions. The eastern sea states (Clusters 1, 2, and 4) account for a combined average of 84.97% of time during the Historical timespan which decreases slightly to 83.53% for

the Future. The corresponding increase in time spent under western sea states (Clusters 3, 5, and 6) indicates that high energy conditions will exist for longer stretches of the extended ice-free season in the future. The weighted combination of all sea states at a specific site can be used to construct a simplified rendition of the unique ice-free seasons across the North Slope during the Historical of Future timespan and the influences from each sea state over time can be evaluated.

Table 5. Time apportionments for Historical and Future Location-Independent centroids. Duration is determined from Energy Occurrence for each sea state.

Site 1	Historical Time Apportionment	Future Time Apportionment	Site 2	Historical Time Apportionment	Future Time Apportionment
Cluster 1	48.66%	51.82%	**Cluster 1**	50.68%	55.05%
Cluster 2	24.93%	20.02%	**Cluster 2**	25.69%	19.04%
Cluster 3	8.75%	13.35%	**Cluster 3**	9.02%	13.03%
Cluster 4	10.01%	8.49%	**Cluster 4**	7.65%	7.32%
Cluster 5	5.68%	3.82%	**Cluster 5**	5.56%	3.69%
Cluster 6	1.97%	2.49%	**Cluster 6**	1.40%	1.86%
Site 3	**Historical Time Apportionment**	**Future Time Apportionment**	**Site 4**	**Historical Time Apportionment**	**Future Time Apportionment**
Cluster 1	53.64%	58.88%	**Cluster 1**	58.96%	64.27%
Cluster 2	23.03%	16.91%	**Cluster 2**	22.94%	16.61%
Cluster 3	12.36%	15.22%	**Cluster 3**	9.27%	12.24%
Cluster 4	2.89%	4.41%	**Cluster 4**	4.17%	3.54%
Cluster 5	7.26%	4.01%	**Cluster 5**	4.29%	2.90%
Cluster 6	0.81%	0.58%	**Cluster 6**	0.36%	0.44%
Site 5	**Historical Time Apportionment**	**Future Time Apportionment**	**Site 6**	**Historical Time Apportionment**	**Future Time Apportionment**
Cluster 1	62.35%	67.28%	**Cluster 1**	73.97%	72.99%
Cluster 2	20.63%	15.91%	**Cluster 2**	13.18%	13.26%
Cluster 3	8.48%	11.41%	**Cluster 3**	6.13%	8.81%
Cluster 4	4.68%	3.19%	**Cluster 4**	1.74%	2.19%
Cluster 5	3.58%	1.95%	**Cluster 5**	4.42%	2.52%
Cluster 6	0.29%	0.26%	**Cluster 6**	0.56%	0.23%

To complement the cluster selections that meet the guidelines in Section 3.3, the Appendix also contains alternative values for the associated parameters in the Historical clusters (Table A2) and the Future clusters (Table A3). Each of these alternatives retains the H_s and T_p values that were calculated following the three Phase k-means routine described in Section 3.1. These alternative clusters do not necessarily follow all of the guidelines outlined in Section 3.3 but allow for a more flexible selection based directly on the data distributions. Most distinctly, the wave and wind orientations were allowed to be sourced from different directions if the T_p value of the cluster

exceeded 8 s. Note that not all cluster parameters differ between the preferred and alternative selections.

5. Discussion

Improved risk assessments rooted in accurate nearshore oceanographic conditions are needed to anticipate coastal dynamics including erosion and flooding. Despite the fact that the Historical (13 years) and Future (20 years) timespans are unequal and too short to capture a full climatology, the purpose of this study is not to quantify exact changes between the timespans but instead to determine simplified descriptions of the boundary conditions that can be used to simulate representative historical and future conditions.

Brute force approaches would require modeling all Historical samples (47,736) and all Future samples (73,568) at each of the six sites: ~100,000 – 700,000 distinct simulations depending on the size of the modeled domain. Initial statistical approaches to establish nearshore oceanographic conditions simulate the entire occurrence diagram shown in Figure 2 (~200 oceanographic conditions to be weighted uniquely for the Historical and Future timespans) for each of the six sites requiring, in total, ~1,200 distinct simulations. Traditional k-means approaches, like those shown in Camus et al. (2011), would require 6 different oceanographic conditions for both the Historical and Future timespans, 12 total, for each of the six sites. Hence, simulation of a minimum of 72 oceanographic conditions would be required. In addition to the computational expense, neither of these methods would produce results that could be used at other locations along the North Slope as all results would be specific to each site.

Using the typological approach, on the other hand, only 12 oceanographic conditions (6 for the Historical and Future timespans each) must be simulated for each bathymetry along the Alaskan North Slope. These simulation outputs can be scaled to each of the six sites as well as having the potential to be used at any other site along the North Slope provided that the appropriate scaling is identified. In total, the typological approach offers a reduction of one to four orders of magnitude in needed simulations (depending upon the approach) to achieve accurate water level and incident wave energy estimates for community-based risk assessments.

Any other region in the world that necessitates a prototypical set of conditions could follow the methodology in Section 3. Reduced order representations of large data sets with prototypical conditions are advantageous for many reasons such as decreased simulation requirements,

decreased experimental requirements, faster design optimization procedures, and increased comprehension of dominant data through fewer, yet prototypical, data.

5.1. A More Energetic Future

Comparison of the AAP flux between Historical and Future conditions at all sites is summarized in Table 6. From this comparison it is clear that there will be increased wave energy with larger increases in the Chukchi (Sites 1 and 2) than the Beaufort Seas (Sites 3-6). The underlying data producing these Chukchi AAP flux values, as shown in Figures A6 and A7, show occurence of H_s up to 4.5- 5.0 m during the 2007-2019 period and 6.5-7.0 m in the future (2020-2040). These match Casas-Prat and Wang (2020b), who show the maximum annual H_s for historical periods in the Chukchi is just under 6 m and growing to 6.5 m in 2081-2100 under RCP8.5. In the Beaufort, Casas-Prat and Wang (2020b) show the maximum annual H_s for historical periods in the Chukchi is 4 m and growing to 6 m in 2081-2100 under RCP8.5. Our simulations reproduce these historical results; Figures 2 and A8-A10 show occurence of H_s up to 3.5-4.5 m during the 2007-2019 timespan. However, during the future timespan, we do not see as drastic of a maximum, due to the fact that our sites do not extend into the deeper areas of the Beaufort, hence Figures 2 and A8-A10 show 4.0-4.5 m annual maximum H_s in the future (2020-2040).

Table 6. Average Annual Power Flux (kW/m) at each site in Historical and Future Timespans.

	Historical AAP flux (kW/m)	Future AAP flux (kW/m)
Site 1	11.38	12.84
Site 2	9.89	11.25
Site 3	5.50	5.93
Site 4	5.47	5.54
Site 5	6.08	5.10
Site 6	3.90	4.25

The increased likelihood of high-valued H_s, T_p, sea states and wind speeds generally observed in the Future typologies are consistent with overall higher energy oceanographic conditions during warmer ocean conditions. For all Future typologies, the T_p increased by an average of 0.23 s and H_s increased by 0.31 m, with only the H_s of Cluster 4 decreasing (from 2.50

m to 2.37 m). These increases match expectations from Casas-Prat and Wang (2020b) who identify that maximum annual H_s should increase between 1.7-2.7 cm/yr in the Beaufort Sea; hence over 20 years, we should expect to see increases between 0.34-0.54 m in maximum annual H_s and although we are investigating centroids and not maxima, these comparative results give increased confidence. Similarly, while the wind speed remained constant for Cluster 1 and actually dropped from 7.5 m/s to 5.0 m/s in Cluster 5, all remaining clusters increased in wind speed by an average of 2.0 m/s in the Future. These increases in typology magnitudes, contributions to AAP flux, and time apportionment suggest that the Future clusters will be more energetic, and even the clusters that represent calmer conditions (Clusters 1 and 2) increase by 2.6% in T_p and 5.1% in H_s.

An important component of our interpretation relies on assessing the influences based on cluster orientation. Following observations about the tendency for the most powerful Arctic storms to come from the west late in the season (Atkinson, 2005), the Future ocean conditions should be defined by stronger, more frequent storms. By defining Clusters 1, 2, and 4 as Eastern (between 24° to 113°) and Clusters 3, 5, and 6 as Western (between 250° to 342°) as introduced in Section 4.4, the Eastern clusters constitute 70.83% of the contributions to AAP flux (C_k) during the Historical timespan but drops to 58.55% of the contributions during the Future. The corresponding increase in energy contribution from the Western clusters (29.17% in the Historical to 41.45% in the Future) is magnified by the findings that the time apportionment increases from 15.03% to 16.47% between the two timespans. The average AAP flux from all sites in the Historical timespan is 7.04 kW/m and increases to 7.48 kW/m in the Future, with only Site 5 experiencing a decrease (from 6.08 kW/m to 5.10 kW/m). Based on the contributions to AAP flux, the Eastern clusters contribute an average of 0.60 kW/m less and the Western clusters contribute 1.05 kW/m more in the Future.

The most drastic changes are observed with regard to the stormiest typology (Cluster 6). While the value of T_p increases by only 3.0% (from 9.90 s to 10.20 s), the H_s for this typology is 31.7% higher (from 3.00 m to 3.95 m) in the Future. The wind speed associated with Cluster 6 also increases from 12.0 m/s to 16.0 m/s. The average contributions to AAP flux for Cluster 6 at all sites increase from 6.9% to 12.3% in the Future timespan. The energy of a sea state will be proportional to the value of H_s^2 and for Cluster 6, the energy associated with this typology will therefore increase by a factor of 1.73 in the future. Additionally, the cumulative storm strength is

measured by the square of the storm's average wind velocity relative to its duration (Atkinson, 2005) and this metric will also increase by a factor of 1.77.

In addition to the elevated contribution to AAP flux, the temporal apportionment for Cluster 6 increases at three of the six sites (Sites 1,2, and 4). Site 6 experiences a significant decrease in storm influence; considering that Site 6 is the farthest eastern site in the study area, it may experience conditions with less influence from the west as it displays the highest occurrence of calm conditions of Cluster 1 for both the Historical (73.97%) and Future (72.99%) timespan (Table 5). As further support for this hypothesis, the two sites located in the Chukchi Sea (Sites 1 and 2) are the only two locations where Cluster 6 occurs more than 1% of the time in both the Historical and Future timespans and this apportionment increases in the Future (Table 5). This shows that the Chukchi side of the North Slope will experience stronger, stormier conditions compared to locations closer to the Beaufort Sea. The diversity of geographic locations in the study area complicates the full interpretation but is necessary to capture the variable conditions along the North Slope.

By including the months of June and December only in the Future data, there is a risk in analyzing more extreme conditions during this timespan that could drive the values for H_s and T_p higher in a biased manner. However, extreme values should be smoothed out as part of the k-means clustering process and the storm intensity and frequency are highest in late summer and early autumn (Erikson et al., 2020) which are shared components of both analyses. The lower sea ice content in the Arctic between August and October allows for increased fetch availability (Barnhart et al., 2014b; Casas-Prat and Wang, 2020b; Lynch and Brunner, 2007; Thomson et al., 2016), leading to longer and stronger storm events over the next two decades that will have the capability to amplify coastal erosion, flooding, and human relocation along the Alaskan coastline as discussed in the next section.

5.2. Typological Application Space

Identification of six typologies that generalize the wave environment along the Arctic coast allows for a simplification of a very complex environmental system. Changes between the Historical and Future typologies demonstrate that we expect the system to become more energetic which will increase the risk of natural hazards along the North Slope. Specifically, the assumed longer ice-free season allows for more frequent storms which coincide with accelerated erosion, onshore inundation, and possible population relocation. According to the DOD, increased storm

intensity and associated storm surge has the potential to disrupt military operations and increase the costs of infrastructure modification and new construction (USGAO, 2014). In order to assess these challenges and to predict the risk associated with different locations along the coast, strategies must be developed that incorporate knowledge of the changing erosion rates (Jones et al., 2009) and flooding amounts.

Erosion

The increased occurrence of higher energy sea states predicted from our analysis is expected to promote greater degrees of coastal erosion during the Future timespan. Erosion along the North Slope of Alaska has increased in response to climate change, with the mean annual erosion rate at Drew Point, Alaska reaching 17.2 m yr^{-1} which is more than twice the historic rate (Jones et al., 2018). More frequent and intense storms during an extended ice-free season will drive greater erosion of the coastline due to thermo-abrasion and thermo-denudation in sensitive areas (Barnhart et al., 2014a; Casas-Prat and Wang, 2020a; Günther et al., 2015; Hequette and Barnes, 1990; Overeem et al., 2011). Arctic communities with populations ranging from 20 to ~6,000 people are not located on state-wide road systems but instead are largely coastal and are accessible only by air or sea (Hamilton et al., 2016). Due to this concentration of settlements near the shore, the expected acceleration of coastal erosion in the Arctic is projected to increase maintenance costs of infrastructure by billions of dollars (Larsen et al., 2008).

In addition to physical removal of material onshore, coastal erosion can rapidly liberate large quantities of frozen organic matter to the coastal ocean (Bristol et al., 2021; Fritz et al., 2017; Stein and Macdonald, 2004; Vonk and Gustafsson, 2013; Vonk et al., 2012). An estimated 5-41 Tg of soil total organic carbon (TOC) is released to the Arctic Ocean each year from coastal erosion, similar in magnitude to river-borne particulate organic carbon (POC) export to the Arctic Ocean (McClelland et al., 2016; Wegner et al., 2015). Mobilizing this once stored source of greenhouse gas can feedback into global warming processes leading to further rises in processes that may accelerate erosion of Arctic coastlines (Barnhart et al., 2014a; Bristol et al., 2021). In addition to carbon, coastal erosion also operates as a flux of nitrogen to the ocean and rapidly increasing erosion rates will accelerate these fluxes in the future (Bristol et al., 2021).

From a case study at Drew Point, winds with velocities above 5 m/s from 240° - 360° and 0° - 90° were significant factors in driving bluff erosion (Jones et al., 2018). Although a simplified, correlative approach, if applied here, we see clusters 1, 5, and 6 meet all of these criteria to be

classified as significant winds in the Historical timespan and for the Future, every cluster now represents a significant wind force. If the entire ice-free season is classified as a combination of the six sea states, coastal bluffs will be subjected to potential erosion at all times in the future. Additionally, the increased water temperatures expected for the Future (simplistically represented in this study as 5.02°C compared to 3.68°C due to data limitations) are expected to increase erosion.

We envision using the typologies as boundary conditions for simulations of coastal erosion (e.g., with the Arctic Coastal Erosion (ACE) model (Bull et al., 2020)) to better link the spatially remote processes that generate ocean waves with the local processes that control their final onshore behavior. The terrestrial component of the ACE model is an advanced finite-element representation of Arctic coastlines that is capable of simulating thermal-chemical-mechanical based erosion in response to episodic, storm-driven boundary conditions (Frederick et al., 2021). Hence this full suite of typological boundary conditions, inclusive of ocean temperature and salinity, will inform erosion rates.

Flooding

Arctic coastal communities are especially prone to flooding in the future due to sea level rise, more frequent storms, and stronger wave energies (Lantz et al., 2020). Additionally, coastal communities along the North Slope are typically located in flat areas that allow for airport construction and marine access (Wicks and Atkinson, 2017) further increasing their susceptibility to flooding. Based on the typical timing of storm events, the potential for coastal flooding along the North Slope has historically been highest during the ice-free season of late summer to early fall (Lynch et al., 2008). Global warming is expected to both raise sea levels and postpone ice formation until later in fall (Terenzi et al., 2014). We anticipate that the combination of longer ice-free seasons, more dominant influences from the west, and elevated wind speeds associated with the clusters will lead to more frequent flooding overall in response to changing oceanographic conditions and that these events will be able to occur later in the ice-free season in the future.

Generally, flooding can be expected when winds sustain a speed of 13 m/s for a duration of 20 hours during the ice-free season (Lynch et al., 2008). The directionality for atmospheric and storm surge model simulations at Barrow between 1950-2003 showed that seven floods were observed, all of which were sourced from the west (between 234° - 320.3°) (Lynch et al., 2008). While the maximum wind speed for the Historical sea states was 13.0 m/s (Cluster 4), two clusters

(Cluster 4 and 6) exceeded this speed in the longer ice-free season for the Future timespan. Cluster 6 additionally has a wave orientation of 280° and wind orientation of 316°, both of which suggest that these conditions will promote flooding along the North Slope in the future.

The increased frequency of extreme events is expected to result in more damaging flooding in the Arctic in response to climate change (Melvin et al., 2017; Radosavljevic et al., 2016) which can further subject the already limited Alaskan roads to settling and subsidence due to flooding-induced thawing of permafrost (Chinowsky et al., 2013). By determining the Location-Dependent time apportionment for each cluster at a given site, we can establish the unique susceptibility of onshore locations to potentially damaging offshore conditions associated with each sea state. We similarly envision using the typologies as boundary conditions for simulations of coastal flooding to better link the spatially remote processes that generate ocean waves with the local processes that control their final onshore behavior and remove the need for correlative wind relationships as the basis of predicting flooding amount.

6. Conclusions

By analyzing oceanographic conditions at six sites along the North Slope of Alaska, we have determined a set of six offshore typologies that are prototypical of conditions that can be used as inputs in nearshore models. Typologies are found by coupling k-means clustering of H_s and T_p with a distribution analysis of associated wave, water, and wind data to produce Location-Independent prototypical boundary conditions for Historical and Future timespans. Analyses of both the Historical and Future conditions confirm the existence of more energetic future ocean conditions characterized by more frequent and higher energy storms. Application of Location-Dependent weightings based on occurrence allows us to apportion the effects of the Location-Independent typologies and analyze changes expected at individual sites. These Location-Independent typologies enable a computationally efficient method to evaluate many nearshore environments that ultimately control the erosion and flooding of coastal regions.

Data Availability Statement

Data associated with this work will be uploaded and permanently hosted through an ESS-DIVE repository upon acceptance of this manuscript.

Acknowledgements

We would like to thank the anonymous reviewers and editor for their constructive comments. We would like to thank Erik Rogers (NRL) for providing the polar stereographic, curvilinear WW3 grid and Ann Dallman (SNL) for providing an initial set of k-means clustering codes upon which we expanded and for a rigorous scientific review. Funding for L. Erikson was provided through the USGS Coastal Marine Geology Program. Support was provided by the US Bureau of Ocean Energy Management through Agreements M17AC00020 (UAF) and M17PG00046 (USGS). Additional support was provided to J. Kasper by the US Bureau of Ocean Energy Management through Cooperative Agreement M17AC00020 (UAF) for the 'Wave and Hydrodynamic Modelling Within the Nearshore Beaufort Sea' project and through NSF Award #1656026 "LTER: Beaufort Sea Lagoons: An Arctic Coastal Ecosystem in Transition." This research was funded as part of the Interdisciplinary Research for Arctic Coastal Environments (InteRFACE) project through the Department of Energy, Office of Science, Biological and Environmental Research RGMA program. This work was additionally supported by the Laboratory Directed Research and Development program at Sandia National Laboratories, a multimission laboratory managed and operated by National Technology and Engineering Solutions of Sandia, LLC., a wholly owned subsidiary of Honeywell International, Inc., for the U.S. Department of Energy's National Nuclear Security Administration under contract DE-NA-0003525.

Supporting Information for "Typological Representation of the Offshore Oceanographic Environment along the Alaskan North Slope"

William K. Eymold[1], Christopher Flanary[2], Li Erikson[3], Kees Nederhoff[4], Christopher C. Chartrand[1], Craig Jones[2], Jeremy Kasper[5], and Diana L. Bull[1*]

[1]*Sandia National Laboratories, Albuquerque, NM 87123, USA*
[2]*Integral Consulting Inc., Santa Cruz, CA 95060, USA*
[3]*US Geological Survey (USGS), Pacific Coastal and Marine Science Center, Santa Cruz, CA 95060, USA*
[4]*Deltares, Delft, The Netherlands*
[5]*University of Alaska Fairbanks, Fairbanks, AK 99775, USA*

**Corresponding author*: dlbull@sandia.gov

Contents

1. Tables A1 – A3
2. Figures A1 – A15

Introduction

Included here are Supplementary Figures A1-A15 and Tables A1-A3 referred to in the manuscript.

References:

Willmott, C.J. (1981) On the Validation of Models. Physical Geography. 2, 184-194

Bull, D.L., Bristol, E.M., Brown, E., Choens, R.C., Connolly, C.T., Flanary, C., Frederick, J.M., Jones, B.M., Jones, C.A., Ward Jones, M., McClelland, J., Mota, A. and Tezaur, I. (2020) Arctic Coastal Erosion: Modeling and Experimentation, SAND2020-10223. Sandia National Laboratories, NM.

Table A1. WW3 Significant Wave Height / Peak Wave Period Performance Metrics across years and sites when forced with ASRv2 reanalysis data. Data compiled from Section 5.2.2 in Bull et al,. 2020.

Station Identifier & General Location	MOB2 (Chukchi)	MOB103 (Chukchi)	ShellHB (Beaufort)	ShellHB (Beaufort)	MOB101 (Chukchi)	MOB102 (Chukchi)
Collection Year	2011 H_s / T_p	2012 H_s / T_p	2012 H_s / T_p	2013 H_s / T_p	2014 H_s / T_p	2015 H_s / T_p
Pearson correlation coefficient	0.85 / 0.68	0.95 / 0.89	0.94 / 0.72	0.85 / 0.49	0.94 / 0.75	0.94 / 0.91
root mean square error RMSE (m / s)	0.31 / 0.9	0.31 / 0.9	0.22 / 1.4	0.29 / 1.8	0.25 / 1.0	0.24 / 0.8
model skill score (Wilmot (1981)	0.92 / 0.81	0.95 / 0.90	0.96 / 0.85	0.91 / 0.71	0.96 / 0.84	0.96 / 0.94

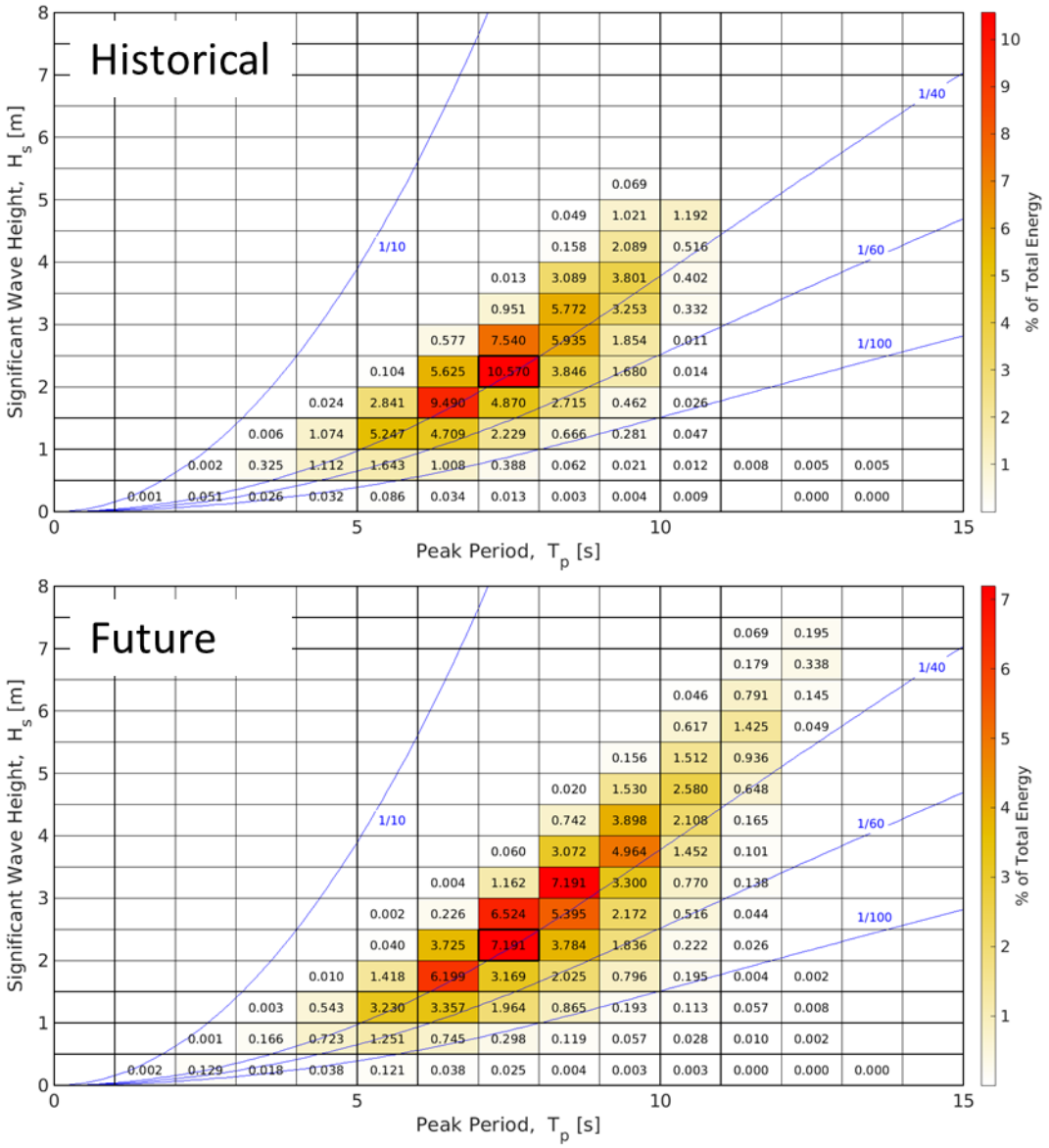

Figure A1. Energy-weighted Occurrence at Site 1 for (top) Historical (2007-2019) and (bottom) Future (2020-2040) time periods. Blue lines indicate constant steepness curves (steepness^{-1} = λ_{Tp}/H_s, where λ_{Tp} is the wavelength of the peak period). Energy-weighted occurrence is represented both numerically and through color.

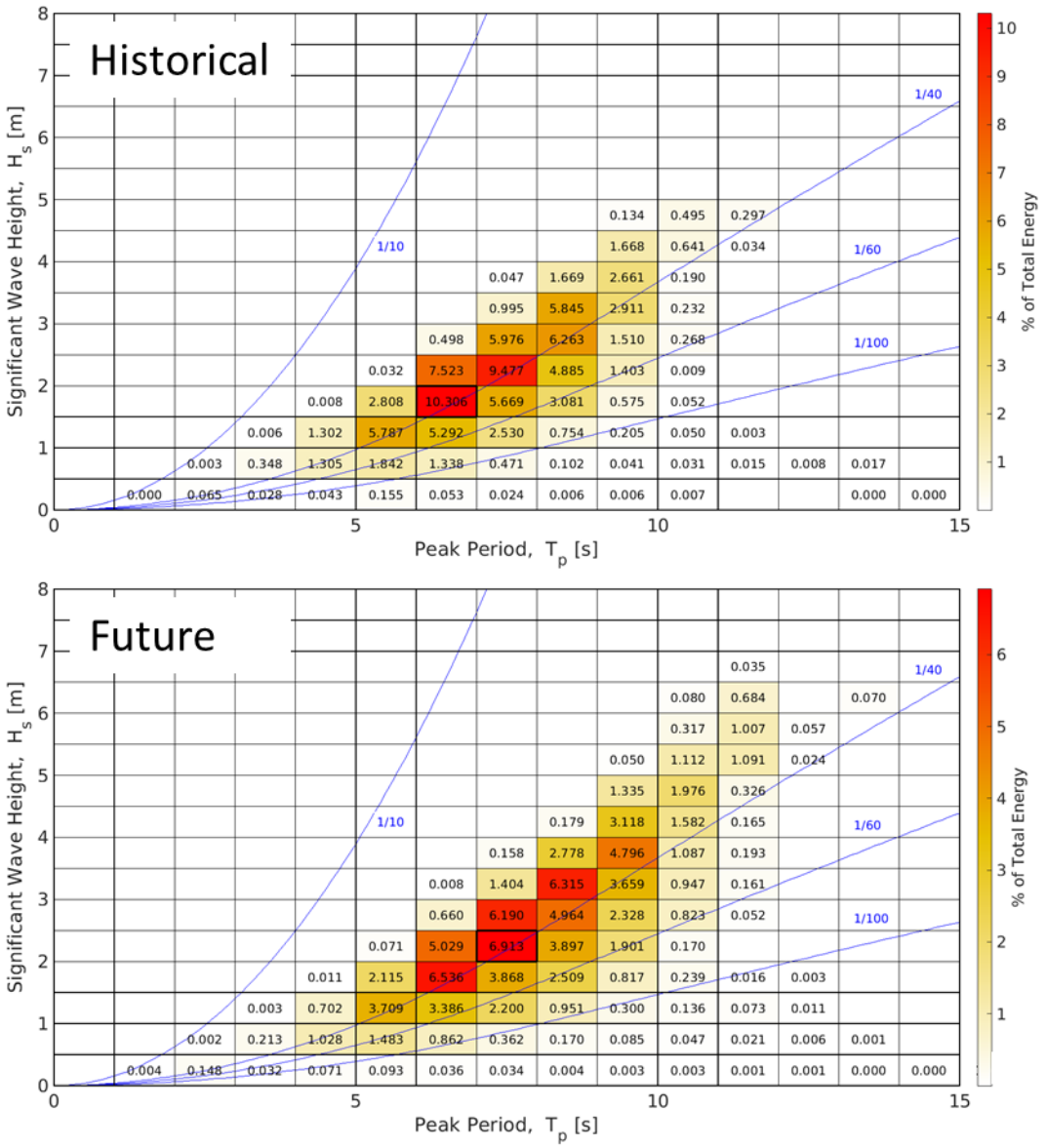

Figure A2. Energy-weighted Occurrence at Site 2 for (top) Historical (2007-2019) and (bottom) Future (2020-2040) time periods. Blue lines indicate constant steepness curves (steepness^{-1} = λ_{Tp}/H_s, where λ_{Tp} is the wavelength of the peak period). Energy-weighted occurrence is represented both numerically and through color.

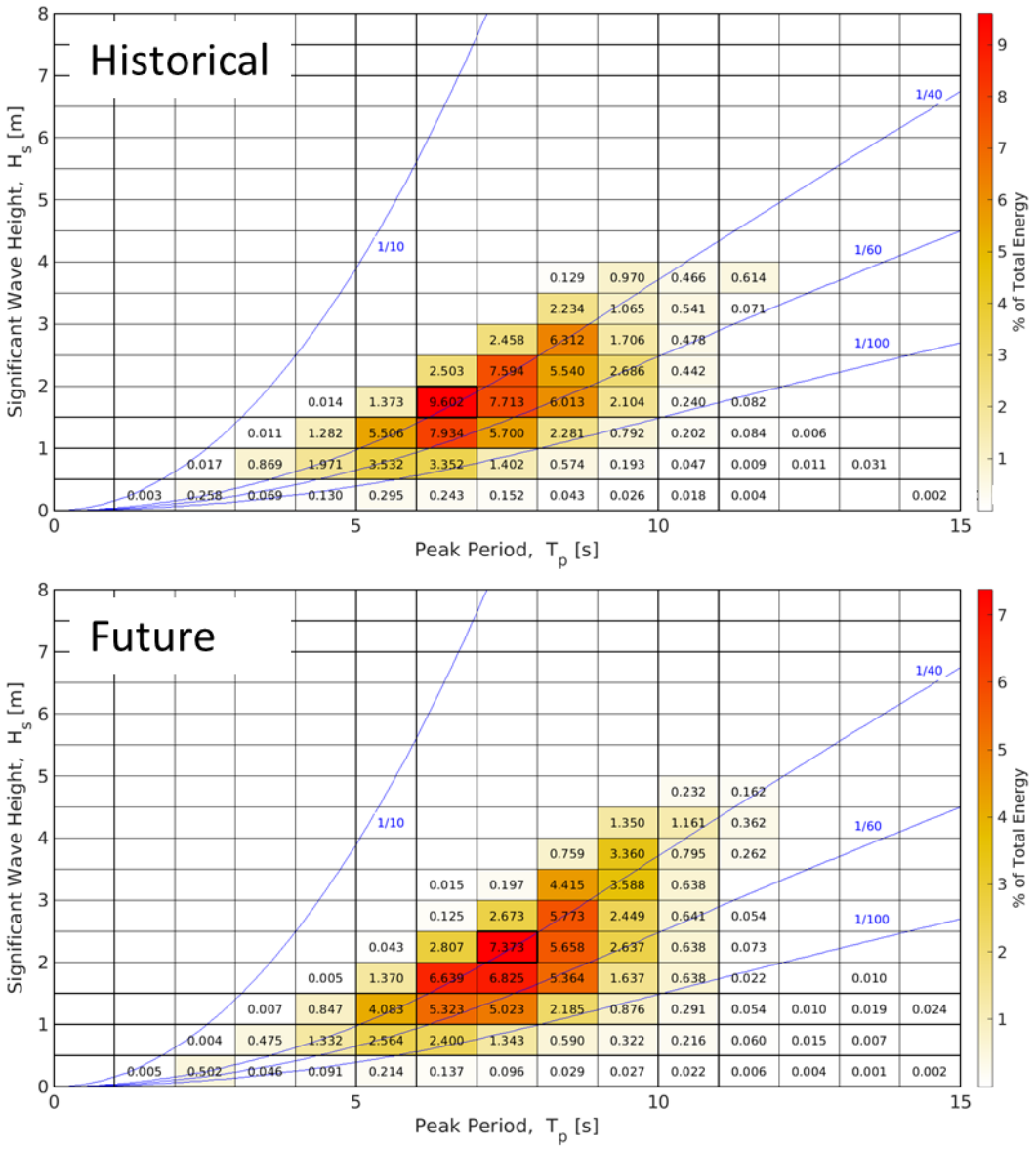

Figure A3. Energy-weighted Occurrence at Site 3 for (top) Historical (2007-2019) and (bottom) Future (2020-2040) time periods. Blue lines indicate constant steepness curves (steepness^{-1} = λ_{Tp}/H_s, where λ_{Tp} is the wavelength of the peak period). Energy-weighted occurrence is represented both numerically and through color.

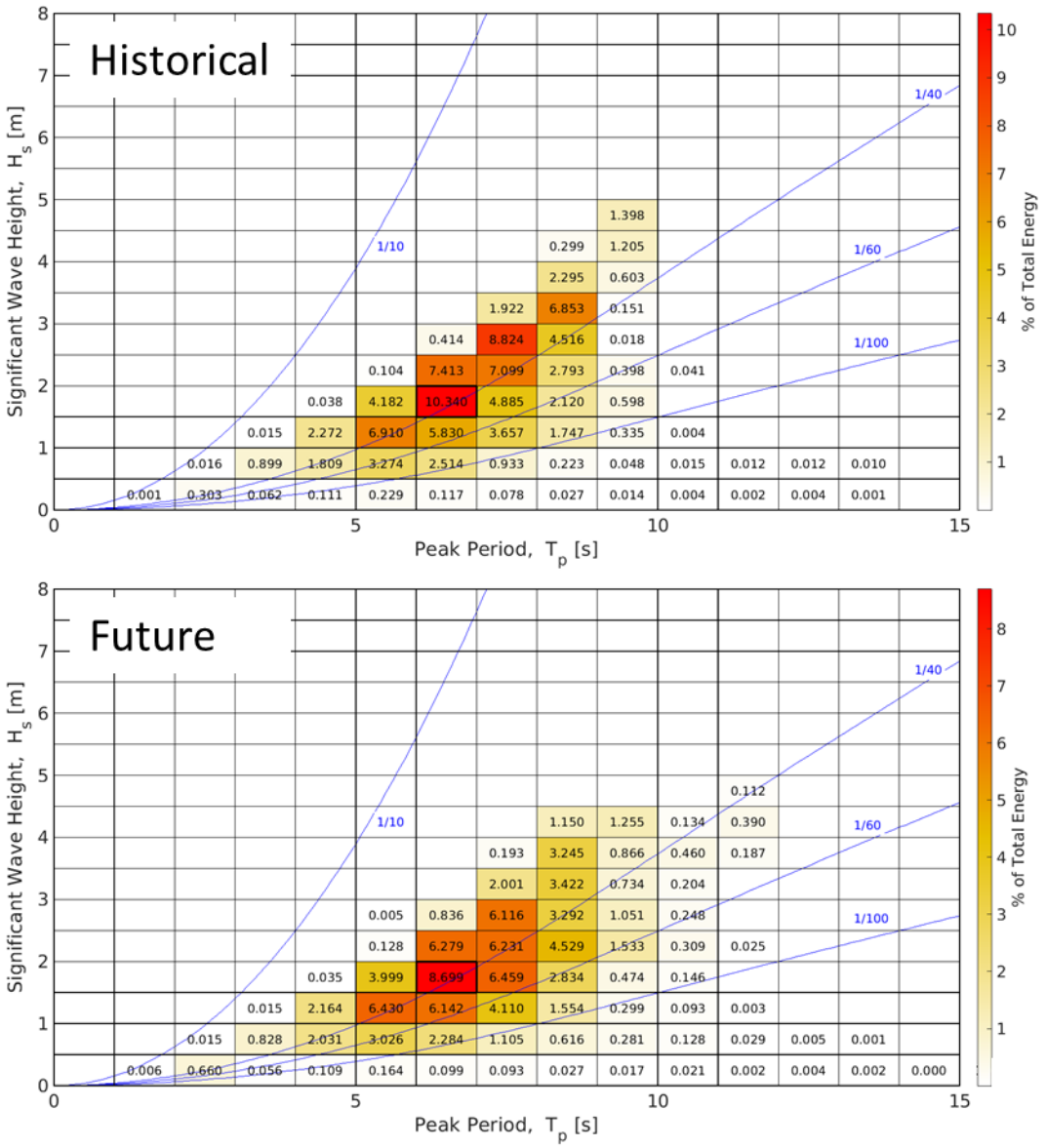

Figure A4. Energy-weighted Occurrence at Site 5 for (top) Historical (2007-2019) and (bottom) Future (2020-2040) time periods. Blue lines indicate constant steepness curves (steepness^{-1} = λ_{Tp}/H_s, where λ_{Tp} is the wavelength of the peak period). Energy-weighted occurrence is represented both numerically and through color.

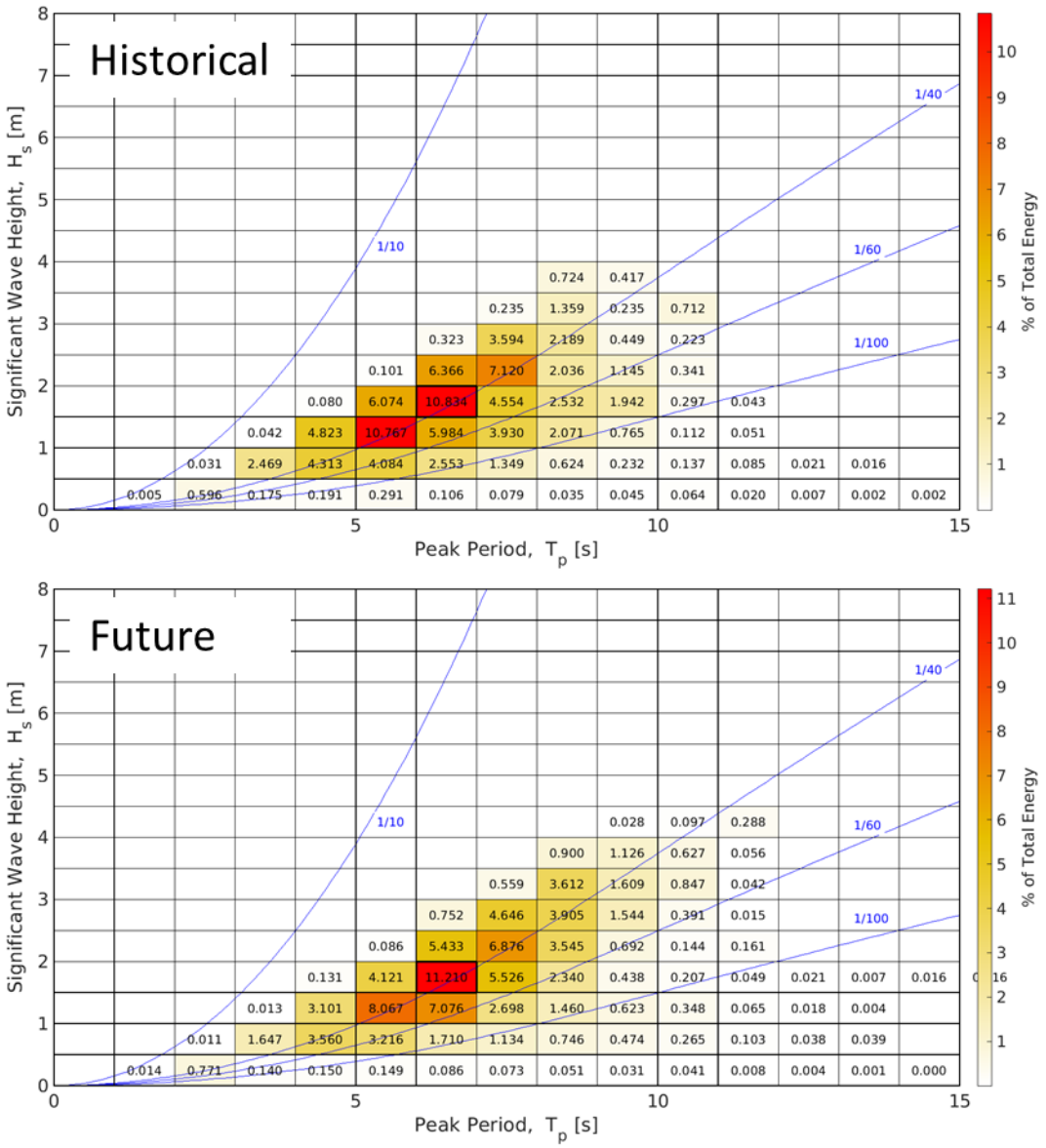

Figure A5. Energy-weighted Occurrence at Site 6 for (top) Historical (2007-2019) and (bottom) Future (2020-2040) time periods. Blue lines indicate constant steepness curves (steepness^{-1} = λ_{Tp}/H_s, where λ_{Tp} is the wavelength of the peak period). Energy-weighted occurrence is represented both numerically and through color.

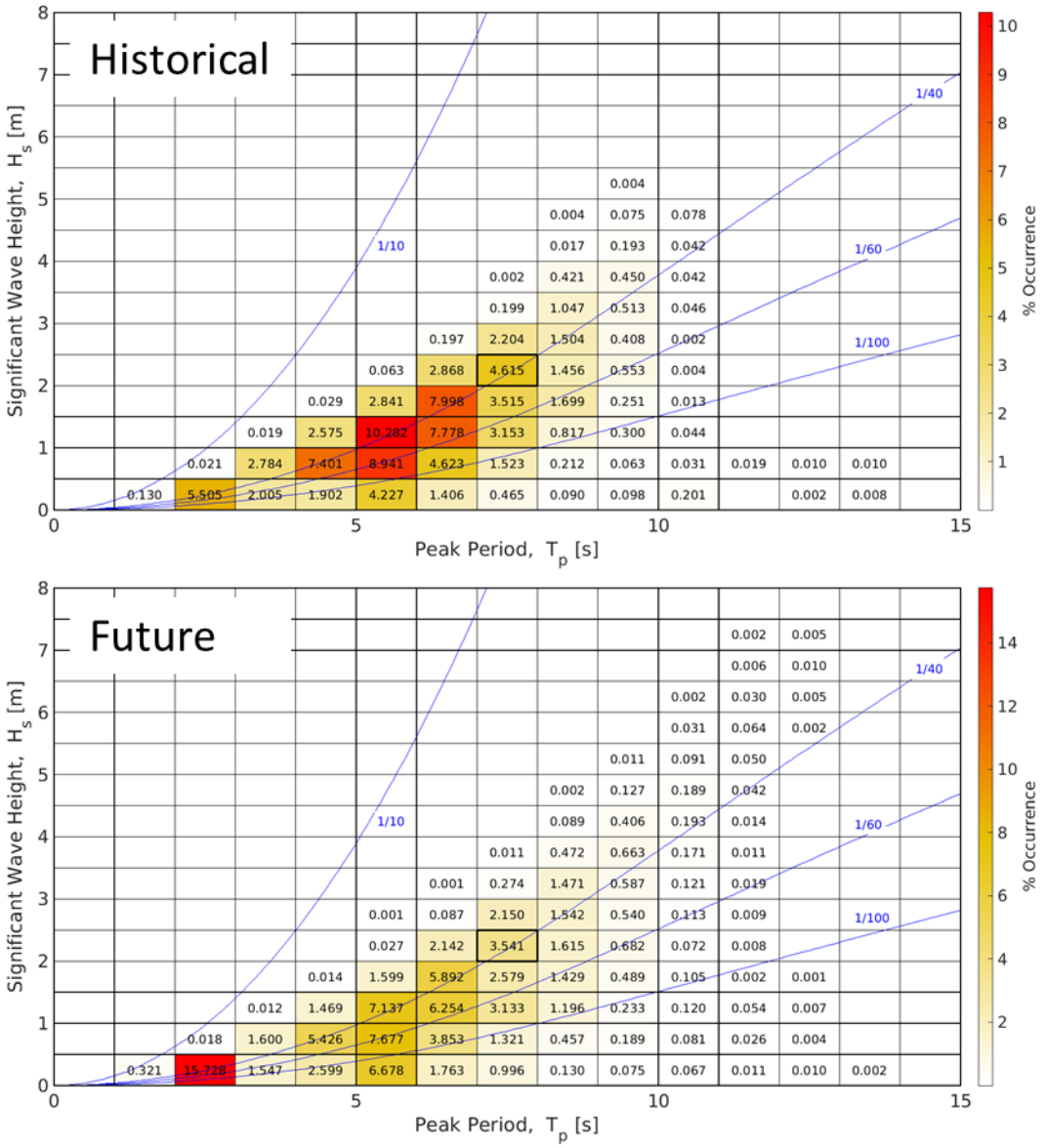

Figure A6. Occurrence JPD at Site 1 for (top) Historical (2007-2019) and (bottom) Future (2020-2040) time periods. Blue lines indicate constant inverse steepness curves (steepness = λ_{Tp}/H_s, where λ_{Tp} is the wavelength of the peak period). Occurrence is represented both numerically and through color.

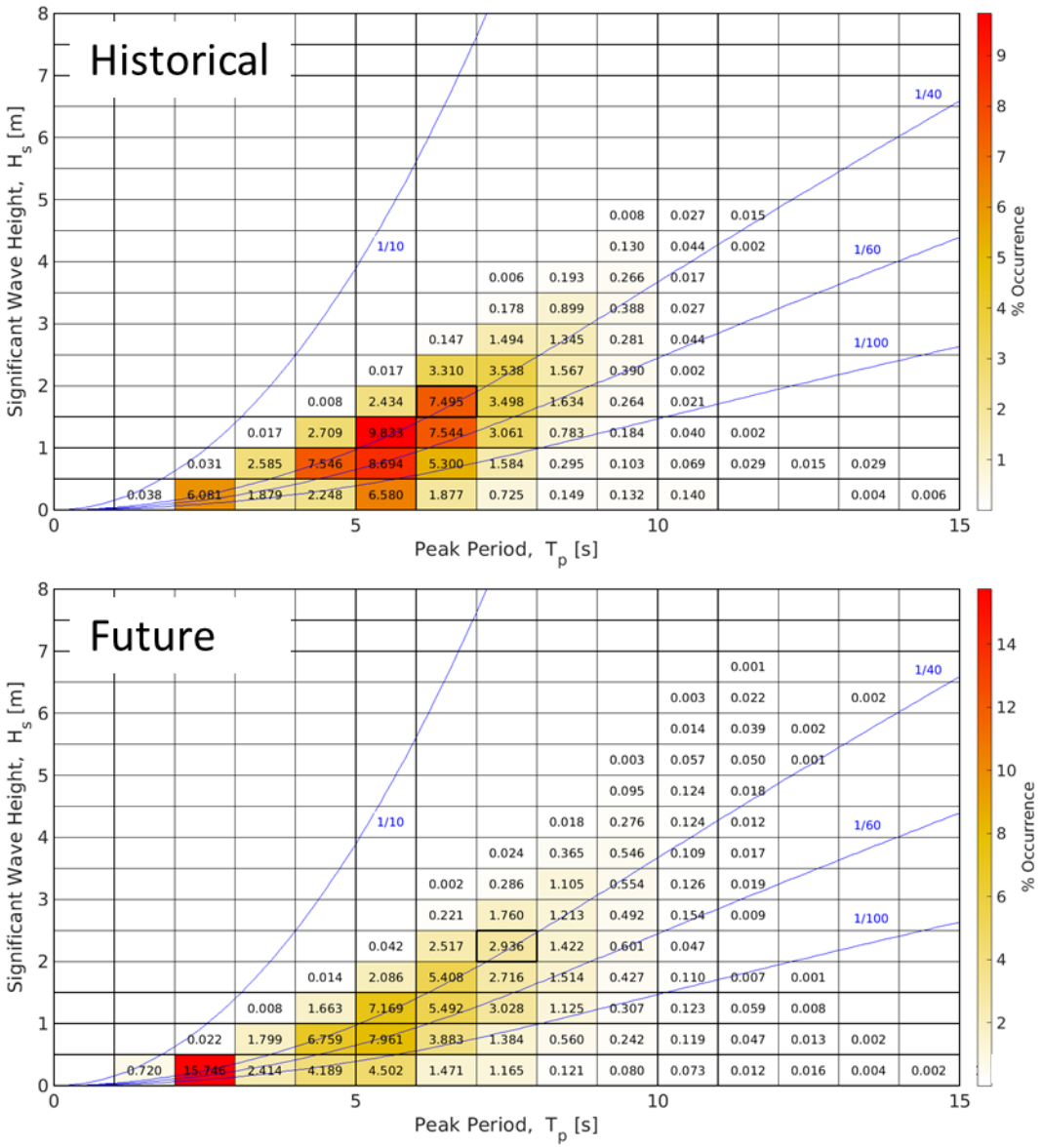

Figure A7. Occurrence JPD at Site 2 for (top) Historical (2007-2019) and (bottom) Future (2020-2040) time periods. Blue lines indicate constant inverse steepness curves (steepness = λ_{Tp}/H_s, where λ_{Tp} is the wavelength of the peak period). Occurrence is represented both numerically and through color.

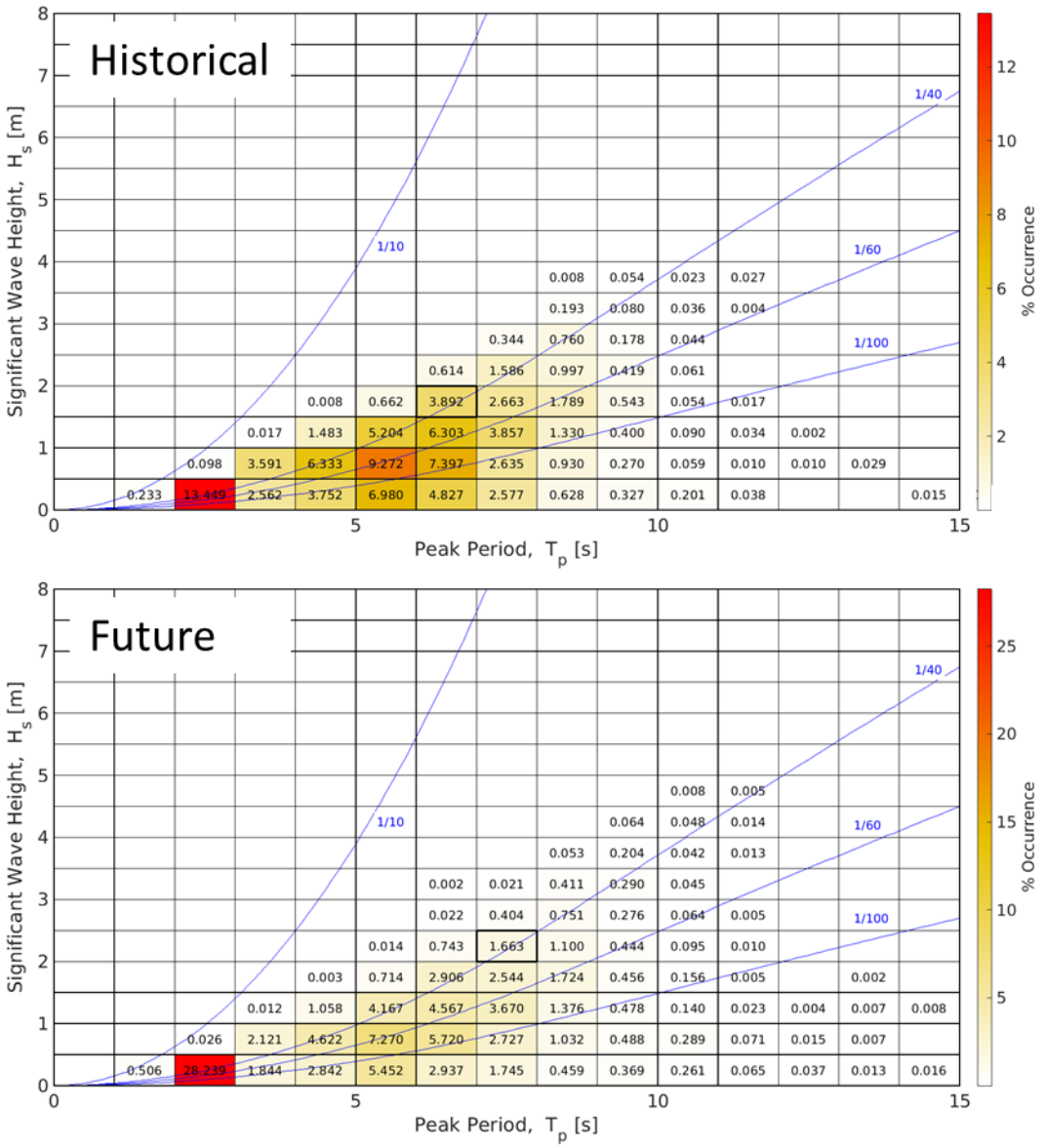

Figure A8. Occurrence JPD at Site 3 for (top) Historical (2007-2019) and (bottom) Future (2020-2040) time periods. Blue lines indicate constant inverse steepness curves (steepness = λ_{Tp}/H_s, where λ_{Tp} is the wavelength of the peak period). Occurrence is represented both numerically and through color.

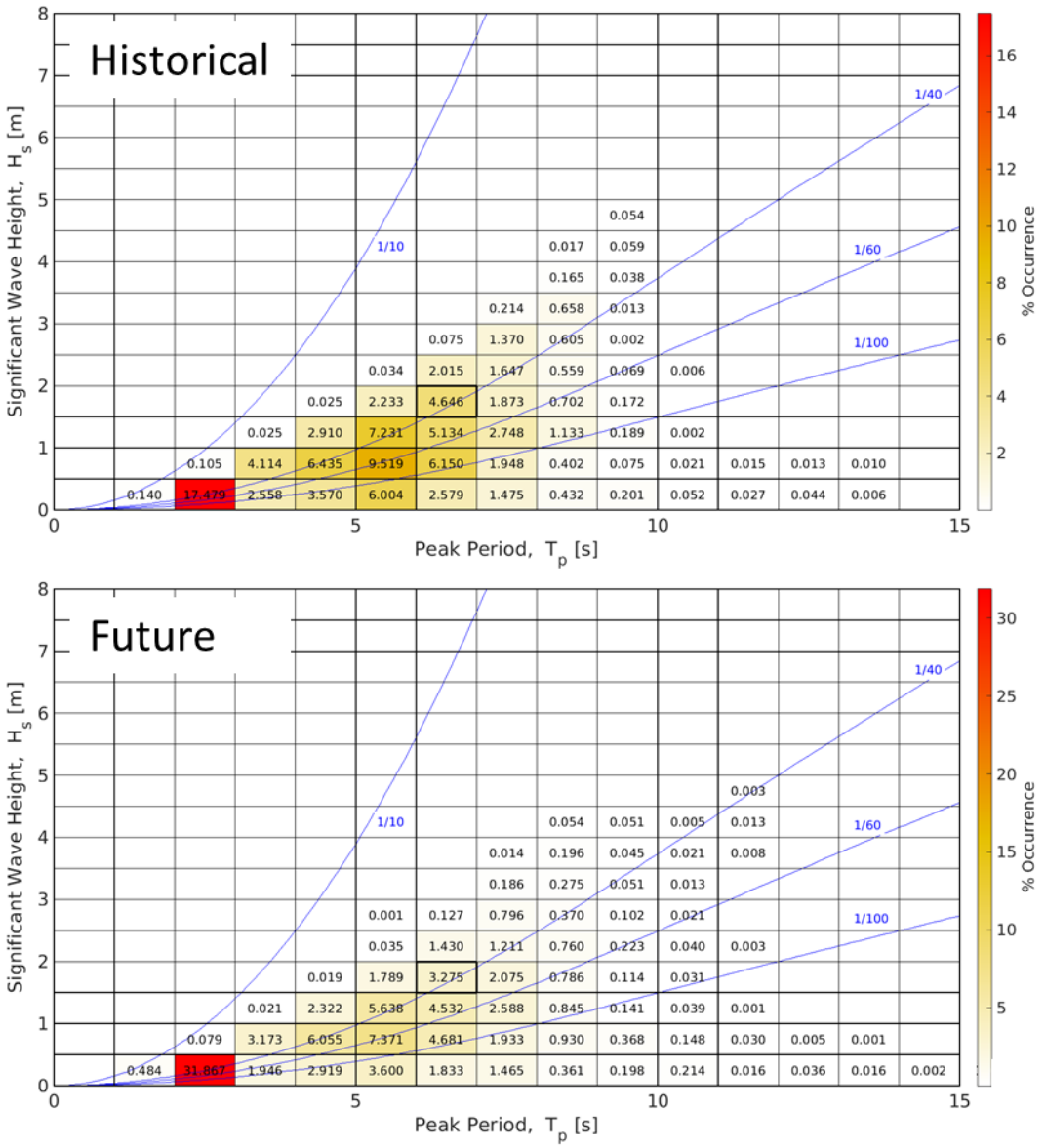

Figure A9. Occurrence JPD at Site 5 for (top) Historical (2007-2019) and (bottom) Future (2020-2040) time periods. Blue lines indicate constant inverse steepness curves (steepness = λ_{Tp}/H_s, where λ_{Tp} is the wavelength of the peak period). Occurrence is represented both numerically and through color.

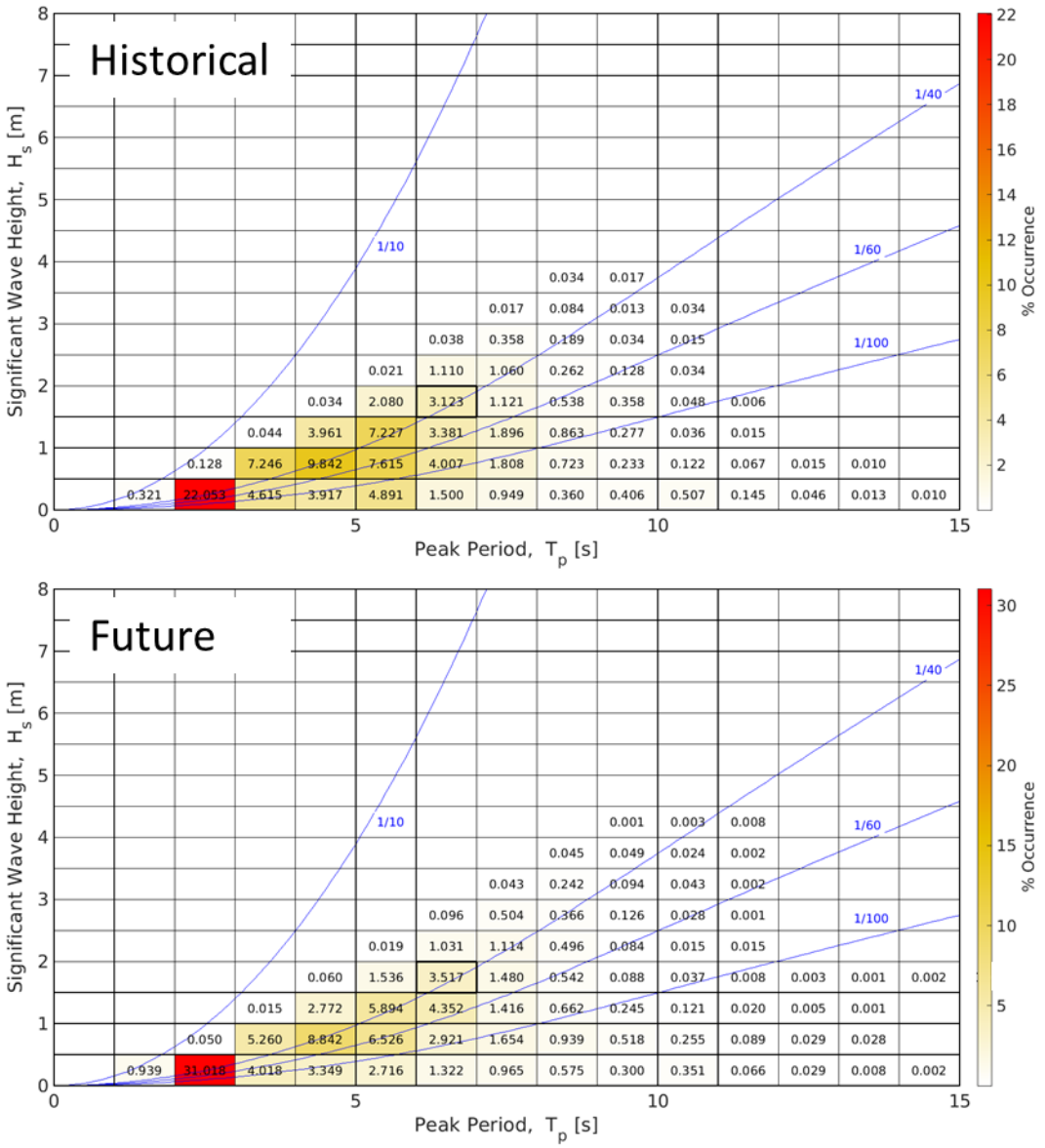

Figure A10. Occurrence JPD at Site 6 for (top) Historical (2007-2019) and (bottom) Future (2020-2040) time periods. Blue lines indicate constant inverse steepness curves (steepness = λ_{Tp}/H_s, where λ_{Tp} is the wavelength of the peak period). Occurrence is represented both numerically and through color.

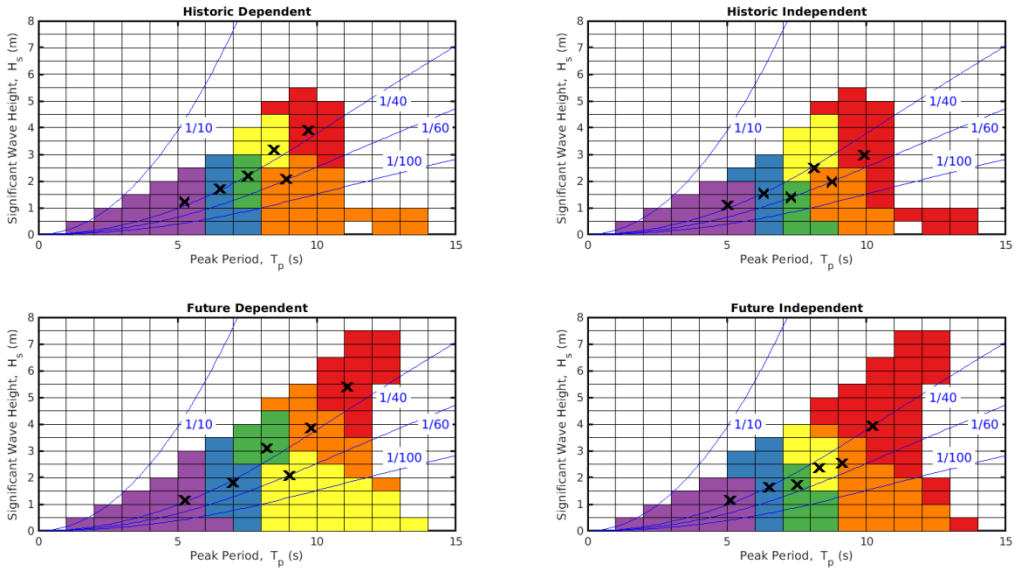

Figure A11. Color coded clusters showing the H_s and T_p bins associated with each cluster at Site 1. Cluster centroids are indicated by the black X in each group. Note that the apportionment of each H_s-T_p bin can change between Historical and Future time spans as well as when clustered using Location Dependent or Location Independent centroids. Compare the bins to those associated with the intensities for the Occurrence and Energy Weighted Occurrence in Figures A1 and A6.

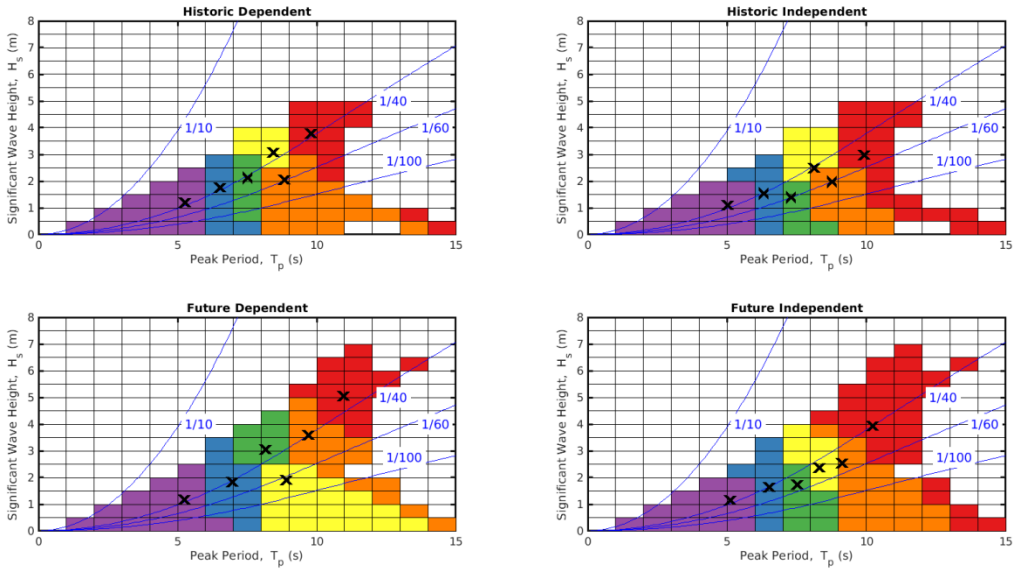

Figure A12. Color coded clusters showing the H_s and T_p bins associated with each cluster at Site 2. Cluster centroids are indicated by the black X in each group. Note that the apportionment of each H_s-T_p bin can change between Historical and Future time spans as well as when clustered using Location Dependent or Location Independent centroids. Compare the bins to those associated with the intensities for the Occurrence and Energy Weighted Occurrence in Figures A2 and A7.

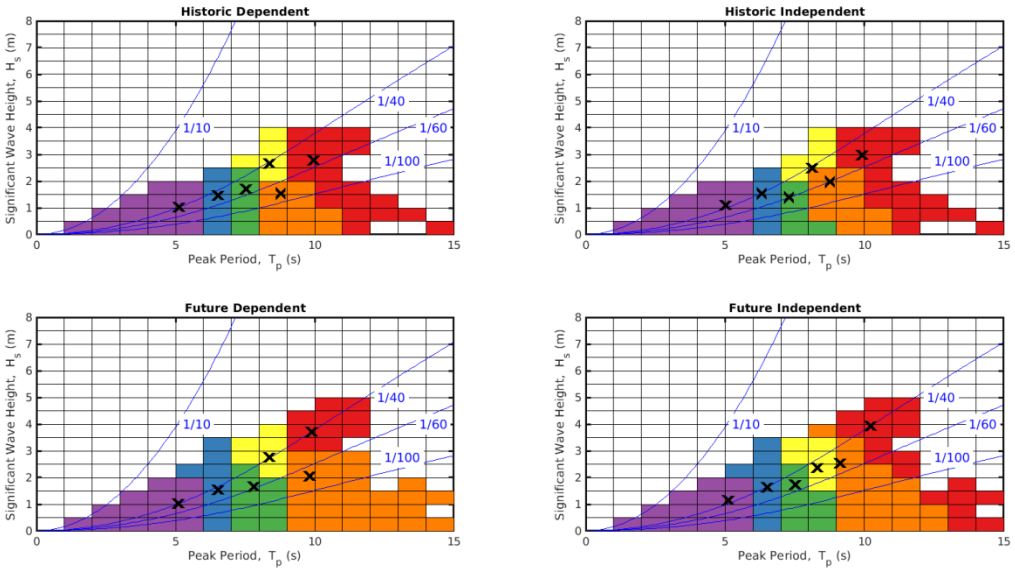

Figure A13. Color coded clusters showing the H_s and T_p bins associated with each cluster at Site 3. Cluster centroids are indicated by the black X in each group. Note that the apportionment of each H_s-T_p bin can change between Historical and Future time spans as well as when clustered using Location Dependent or Location Independent centroids. Compare the bins to those associated with the intensities for the Occurrence and Energy Weighted Occurrence in Figures A3 and A8.

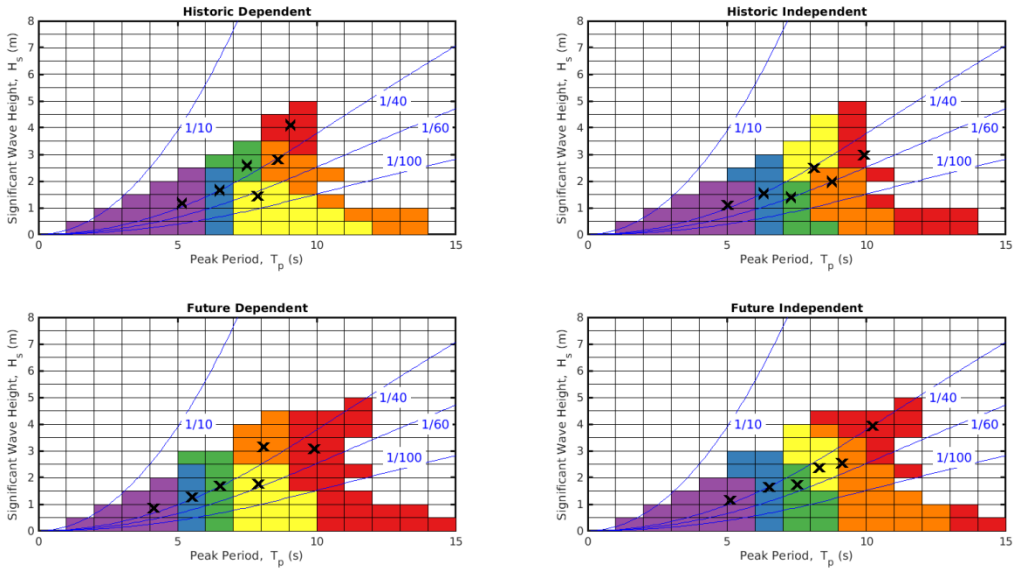

Figure A14. Color coded clusters showing the H_s and T_p bins associated with each cluster at Site 5. Cluster centroids are indicated by the black X in each group. Note that the apportionment of each H_s-T_p bin can change between Historical and Future time spans as well as when clustered using Location Dependent or Location Independent centroids. Compare the bins to those associated with the intensities for the Occurrence and Energy Weighted Occurrence in Figures A4 and A9.

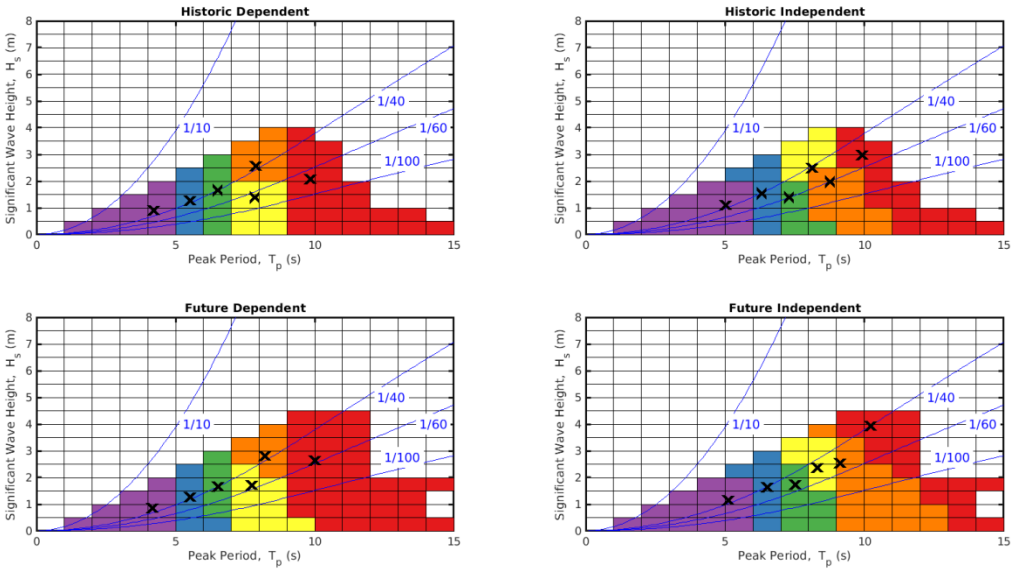

Figure A15. Color coded clusters showing the H_s and T_p bins associated with each cluster at Site 6. Cluster centroids are indicated by the black X in each group. Note that the apportionment of each H_s-T_p bin can change between Historical and Future time spans as well as when clustered using Location Dependent or Location Independent centroids. Compare the bins to those associated with the intensities for the Occurrence and Energy Weighted Occurrence in Figures A5 and A10.

Table A2. Alternative parameters associated with each cluster for the Historical timespan.

Historic	Tp (s)	Hs (m)	Wave Direction	Water Level (m)	Wind Direction	Wind Speed (m/s)	Wave-Wind Orientation
Cluster 1	5.00	1.11	33	-0.15	29	5.00	N-N
Cluster 2	6.30	1.55	0	-0.10	100	6.00	N-E
Cluster 3	7.30	1.40	260	-0.05	225	4.75	W-W
Cluster 4	8.10	2.50	240	-0.20	45	12.00	W-E
Cluster 5	8.75	2.00	100	+0.05	270	6.75	E-W
Cluster 6	9.90	3.00	110	-0.10	120	13.00	E-E

Table A3. Alternative parameters associated with each cluster for the Future timespan.

Future	Tp (s)	Hs (m)	Wave Direction	Water Level (m)	Wind Direction	Wind Speed (m/s)	Wave-Wind Orientation
Cluster 1	5.10	1.15	300	-0.05	315	4.80	W-W
Cluster 2	6.50	1.65	75	+0.05	80	8.00	E-E
Cluster 3	7.50	1.75	80	+0.10	90	7.00	E-E
Cluster 4	8.30	2.37	61	-0.10	53	13.00	E-E
Cluster 5	9.10	2.55	75	+0.20	210	4.00	E-W
Cluster 6	10.20	3.95	280	-0.20	342	16.00	W-W

References

Abadie, S., Butel, R., Mauriet, S., Morichon, D. and Dupuis, H. (2006) Wave climate and longshore drift on the South Aquitaine coast. Continental Shelf Research 26, 1924-1939.

Amante, C. and Eakins, B.W. (2009) ETOPO1 arc-minute global relief model: procedures, data sources and analysis.

Atkinson, D.E. (2005) Observed storminess patterns and trends in the circum-Arctic coastal regime. Geo-Marine Letters 25, 98-109.

Barnhart, K.R., Anderson, R.S., Overeem, I., Wobus, C., Clow, G.D. and Urban, F.E. (2014a) Modeling erosion of ice-rich permafrost bluffs along the Alaskan Beaufort Sea coast. Journal of Geophysical Research: Earth Surface 119, 1155-1179.

Barnhart, K.R., Overeem, I. and Anderson, R.S. (2014b) The effect of changing sea ice on the physical vulnerability of Arctic coasts. The Cryosphere 8, 1777-1799.

Bieniek, P.A., Bhatt, U.S., Walsh, J.E., Rupp, T.S., Zhang, J., Krieger, J.R. and Lader, R. (2016) Dynamical downscaling of ERA-Interim temperature and precipitation for Alaska. Journal of Applied Meteorology and Climatology 55, 635-654.

Bilskie, M., Hagen, S., Medeiros, S. and Passeri, D. (2014) Dynamics of sea level rise and coastal flooding on a changing landscape. Geophysical Research Letters 41, 927-934.

Bristol, E.M., Connolly, C.T., Lorenson, T.D., Richmond, B.M., Ilgen, A.G., Choens, R.C., Bull, D.L., Kanevskiy, M., Iwahana, G., Jones, B.M. and McClelland, J.W. (2021) Geochemistry of coastal permafrost and erosion-driven organic matter fluxes to the Beaufort Sea near Drew Point, Alaska. Frontiers in Earth Science 8, 639.

Bromwich, D., Wilson, A., Bai, L., Liu, Z., Barlage, M., Shih, C.-F., Maldonado, S., Hines, K., Wang, S.-H. and Woollen, J. (2018) The Arctic System Reanalysis, Version 2. Bulletin of the American Meteorological Society 99, 805-828.

Bronen, R. and Chapin, F.S. (2013) Adaptive governance and institutional strategies for climate-induced community relocations in Alaska. Proceedings of the National Academy of Sciences 110, 9320-9325.

Bull, D. and Dallman, A. (2017) Wave Energy Prize experimental sea state selection, International Conference on Offshore Mechanics and Arctic Engineering. American Society of Mechanical Engineers, p. V010T009A025.

Bull, D.L., Bristol, E.M., Brown, E., Choens, R.C., Connolly, C.T., Flanary, C., Frederick, J.M., Jones, B.M., Jones, C.A., Ward Jones, M., McClelland, J., Mota, A. and Tezaur, I. (2020) Arctic Coastal Erosion: Modeling and Experimentation, SAND2020-10223. Sandia National Laboratories, NM.

Cahill, B. and Lewis, T. (2013) Wave energy resource characterisation of the Atlantic marine energy test site. International Journal of Marine Energy 1, 3-15.

Camus, P., Mendez, F.J., Medina, R. and Cofiño, A.S. (2011) Analysis of clustering and selection algorithms for the study of multivariate wave climate. Coastal Engineering 58, 453-462.

Casas-Prat, M. and Wang, X.L. (2020a) Projections of extreme ocean waves in the Arctic and potential implications for coastal inundation and erosion. Journal of Geophysical Research: Oceans 125, e2019JC015745.

Casas-Prat, M. and Wang, X.L.J.G.R.L. (2020b) Sea ice retreat contributes to projected increases in extreme Arctic Ocean surface waves. 47, e2020GL088100.

Chakrabarti, S.K. (1987) Hydrodynamics of Offshore Structures. WIT press.

Chinowsky, P.S., Price, J.C. and Neumann, J.E. (2013) Assessment of climate change adaptation costs for the US road network. Global Environmental Change 23, 764-773.
Copernicus Climate Change Service Climate (C3S) (2017) ERA5: Fifth generation of ECMWF atmospheric reanalyses of the global climate. Copernicus Climate Change Service Climate Data Store (CDS).
Cummings, J.A. (2005) Operational multivariate ocean data assimilation. Quarterly Journal of the Royal Meteorological Society: A journal of the atmospheric sciences, applied meteorology and physical oceanography 131, 3583-3604.
Cummings, J.A. and Smedstad, O.M. (2013) Variational data assimilation for the global ocean, Data Assimilation for Atmospheric, Oceanic and Hydrologic Applications (Vol. II). Springer, pp. 303-343.
Dallman, A.R. and Neary, V.S. (2014) Characterization of US Wave Energy Converter (WEC) Test Sites: A Catalogue of Met-Ocean Data. Sandia National Lab.(SNL-NM), Albuquerque, NM (United States).
Day, J.J. and Hodges, K.I. (2018) Growing land-sea temperature contrast and the intensification of Arctic cyclones. Geophysical Research Letters 45, 3673-3681.
Deltares (2018a) Delft3D-FLOW: Simulation of multi-dimensional hydrodynamic flows and transport phenomena, including sediments: User Manual. Deltares, The Netherlands.
Deltares (2018b) Delft3D-WAVE: Simulation of short-crested waves with SWAN: User Manual. Deltares, The Netherlands. .
Donner, L.J., Wyman, B.L., Hemler, R.S., Horowitz, L.W., Ming, Y., Zhao, M., Golaz, J.-C., Ginoux, P., Lin, S.-J. and Schwarzkopf, M.D. (2011) The dynamical core, physical parameterizations, and basic simulation characteristics of the atmospheric component AM3 of the GFDL global coupled model CM3. Journal of Climate 24, 3484-3519.
Erikson, L.H., Gibbs, A.E., Richmond, B.M., Storlazzi, C.D., Jones, B.M. and Ohman, K. (2020) Changing storm conditions in response to projected 21st century climate change and the potential impact on an arctic barrier island–lagoon system—A pilot study for Arey Island and Lagoon, eastern Arctic Alaska. US Geological Survey.
Erikson, L.H., Hegermiller, C.E., Barnard, P.L. and Storlazzi, C.D. (2016) Wave Projections for United States Mainland Coasts. US Geological Survey pamphlet to accompany Data Release.
Frederick, J., Mota, A., Tezaur, I. and Bull, D. (2021) A thermo-mechanical terrestrial model of Arctic coastal erosion. Journal of Computational and Applied Mathematics 397, 113533.
Fritz, M., Vonk, J.E. and Lantuit, H. (2017) Collapsing Arctic Coastlines. Nature Climate Change 7, 6-7.
Garratt, J. (1977) Review of drag coefficients over oceans and continents. Monthly Weather Review 105, 915-929.
Griffies, S.M., Winton, M., Donner, L.J., Horowitz, L.W., Downes, S.M., Farneti, R., Gnanadesikan, A., Hurlin, W.J., Lee, H.-C. and Liang, Z. (2011) The GFDL CM3 coupled climate model: characteristics of the ocean and sea ice simulations. Journal of Climate 24, 3520-3544.
Griffiths, W., Schmidt, D., Fechhelm, R., Gallaway, B., Dillinger Jr, R., Gazey, W., Neill, W. and Baker, J. (1983) Environmental Summer Studies (1982) for the Endicott Development, Vol. 3. Report by LGL Alaska Research Associates, Inc., and Northern Technical Services, for Sohio Alaska Petroleum Company, Anchorage, AK.
Günther, F., Overduin, P.P., Yakshina, I.A., Opel, T., Baranskaya, A.V. and Grigoriev, M.N.J.T.C. (2015) Observing Muostakh disappear: permafrost thaw subsidence and erosion

of a ground-ice-rich island in response to arctic summer warming and sea ice reduction. 9, 151-178.
Hachmeister, L.E., Short, K.S., Schrader, G.C., Winnick, K.B., and Johannessen, J.W. (1985) Oceanographic Monitoring. Endicott Environmental Studies. Envirosphere Company, Bellevue, WA.
Hamilton, A.I., Gibbs, A.E., Erikson, L.H. and Engelstad, A.C. (2021) Assessment of barrier island morphological change in northern Alaska. US Geological Survey.
Hamilton, L.C., Saito, K., Loring, P.A., Lammers, R.B. and Huntington, H.P. (2016) Climigration? Population and climate change in Arctic Alaska. Population and Environment 38, 115-133.
Hegermiller, C., Antolinez, J.A., Rueda, A., Camus, P., Perez, J., Erikson, L.H., Barnard, P.L. and Mendez, F.J. (2017) A multimodal wave spectrum–based approach for statistical downscaling of local wave climate. Journal of Physical Oceanography 47, 375-386.
Hequette, A. and Barnes, P.W.J.M.G. (1990) Coastal retreat and shoreface profile variations in the Canadian Beaufort Sea. 91, 113-132.
Holthuijsen, L.H. (2010) Waves in Oceanic and Coastal Waters. Cambridge University Press.
Irrgang, A.M., Bendixen, M., Farquharson, L.M., Baranskaya, A.V., Erikson, L.H., Gibbs, A.E., Ogorodov, S.A., Overduin, P.P., Lantuit, H., Grigoriev, M.N.J.N.R.E. and Environment (2022) Drivers, dynamics and impacts of changing Arctic coasts. 3, 39-54.
Jin, F.-F. (1997) An equatorial ocean recharge paradigm for ENSO. Part I: Conceptual model. Journal of the Atmospheric Sciences 54, 811-829.
Jones, B.M., Arp, C.D., Jorgenson, M.T., Hinkel, K.M., Schmutz, J.A. and Flint, P.L. (2009) Increase in the rate and uniformity of coastline erosion in Arctic Alaska. Geophysical Research Letters 36.
Jones, B.M., Farquharson, L.M., Baughman, C.A., Buzard, R.M., Arp, C.D., Grosse, G., Bull, D.L., Günther, F., Nitze, I. and Urban, F. (2018) A decade of remotely sensed observations highlight complex processes linked to coastal permafrost bluff erosion in the Arctic. Environmental Research Letters 13, 115001.
Joyce, B.R., Pringle, W.J., Wirasaet, D., Westerink, J.J., Van der Westhuysen, A.J., Grumbine, R. and Feyen, J. (2019) High resolution modeling of western Alaskan tides and storm surge under varying sea ice conditions. Ocean Modelling 141, 101421.
Kernkamp, H.W., Van Dam, A., Stelling, G.S. and de Goede, E.D. (2011) Efficient scheme for the shallow water equations on unstructured grids with application to the Continental Shelf. Ocean Dynamics 61, 1175-1188.
Lantz, T.C., Moffat, N.D., Jones, B.M., Chen, Q. and Tweedie, C.E. (2020) Mapping exposure to flooding in three coastal communities on the North slope of Alaska using Airborne LiDAR. Coastal Management 48, 96-117.
Larsen, P.H., Goldsmith, S., Smith, O., Wilson, M.L., Strzepek, K., Chinowsky, P. and Saylor, B. (2008) Estimating future costs for Alaska public infrastructure at risk from climate change. Global Environmental Change 18, 442-457.
Lavelle, J. and Kofoed, J.P. (2013) Representative spectra of the wave resource from real sea wave measurements, European Wave and Tidal Energy Conference. Technical Committee of the European Wave and Tidal Energy Conference.
Lenee-Bluhm, P., Paasch, R. and Özkan-Haller, H.T. (2011) Characterizing the wave energy resource of the US Pacific Northwest. Renewable Energy 36, 2106-2119.

Lüpkes, C., Gryanik, V.M., Hartmann, J. and Andreas, E.L. (2012) A parametrization, based on sea ice morphology, of the neutral atmospheric drag coefficients for weather prediction and climate models. Journal of Geophysical Research: Atmospheres 117.

Lyard, F., Lefevre, F., Letellier, T. and Francis, O. (2006) Modelling the global ocean tides: modern insights from FES2004. Ocean Dynamics 56, 394-415.

Lynch, A.H. and Brunner, R.D. (2007) Context and climate change: an integrated assessment for Barrow, Alaska. Climatic Change 82, 93-111.

Lynch, A.H., Lestak, L.R., Uotila, P., Cassano, E.N. and Xie, L. (2008) A factorial analysis of storm surge flooding in Barrow, Alaska. Monthly Weather Review 136, 898-912.

Manson, G.K. and Solomon, S.M. (2007) Past and future forcing of Beaufort Sea coastal change. Atmosphere-Ocean 45, 107-122.

McClelland, J., Holmes, R., Peterson, B., Raymond, P., Striegl, R., Zhulidov, A., Zimov, S., Zimov, N., Tank, S. and Spencer, R. (2016) Particulate organic carbon and nitrogen export from major Arctic rivers. Global Biogeochemical Cycles 30, 629-643.

Melvin, A.M., Larsen, P., Boehlert, B., Neumann, J.E., Chinowsky, P., Espinet, X., Martinich, J., Baumann, M.S., Rennels, L. and Bothner, A. (2017) Climate change damages to Alaska public infrastructure and the economics of proactive adaptation. Proceedings of the National Academy of Sciences 114, E122-E131.

Meredith, M., Sommerkorn, M., Cassotta, S., Derksen, C., Ekaykin, A., Hollowed, A., Kofinas, G., Mackintosh, A., Melbourne-Thomas, J. and Muelbert, M. (2019) Polar Regions. Chapter 3, IPCC Special Report on the Ocean and Cryosphere in a Changing Climate.

Ochi, M. (1998) Ocean Waves: The Stochastic Approach. Oceanographic Literature Review 6, 904.

Overeem, I., Anderson, R.S., Wobus, C.W., Clow, G.D., Urban, F.E. and Matell, N. (2011) Sea ice loss enhances wave action at the Arctic coast. Geophysical Research Letters 38.

Overland, J., Dunlea, E., Box, J.E., Corell, R., Forsius, M., Kattsov, V., Olsen, M.S., Pawlak, J., Reiersen, L.-O. and Wang, M. (2019) The urgency of Arctic change. Polar Science 21, 6-13.

Palinkas, L.A. (2020) Fleeing Coastal Erosion: Kivalina and Isle de Jean Charles, Global Climate Change, Population Displacement, and Public Health. Springer, pp. 127-145.

Perovich, D.K., Meier, W., Tschudi, M., Farrell, S., Hendricks, S., Gerland, S., Haas, C., Krumpen, T., Polashenski, R., Ricker, R., Webster, M. (2018) Sea Ice. [in Arctic Report Card 2018], https://arctic.noaa.gov/Report-Card.

Pond, S. and Pickard, G.L. (1983) Introductory Dynamical Oceanography. Gulf Professional Publishing.

Radosavljevic, B., Lantuit, H., Pollard, W., Overduin, P., Couture, N., Sachs, T., Helm, V. and Fritz, M. (2016) Erosion and flooding—threats to coastal infrastructure in the Arctic: a case study from Herschel Island, Yukon Territory, Canada. Estuaries and Coasts 39, 900-915.

Ravens, T.M., Jones, B.M., Zhang, J., Arp, C.D. and Schmutz, J.A. (2012) Process-based coastal erosion modeling for drew point, North Slope, Alaska. Journal of Waterway, Port, Coastal, and Ocean Engineering 138, 122-130.

Reguero, B., Méndez, F. and Losada, I. (2013) Variability of multivariate wave climate in Latin America and the Caribbean. Global and Planetary Change 100, 70-84.

Reimnitz, E. and Maurer, D.K. (1979) Effects of storm surges on the Beaufort Sea coast, northern Alaska. Arctic, 329-344.

Ristroph, E.B. (2021) Navigating climate change adaptation assistance for communities: a case study of Newtok Village, Alaska. Journal of Environmental Studies and Sciences 11, 329-340.

Rogers, W.E. and Zieger, S. (2014) New wave-ice interaction physics in Wavewatch III®, 22nd IAHR International Symposium on Ice. International Association for Hydro-environment Engineering and Research (IAHR), Singapore.

Stansby, P., Zhou, J., Kuang, C., Walkden, M., Hall, J., Dickson, M. and Research., I.t.T.C.f.C.C. (2007) Long-term prediction of nearshore wave climate with an application to cliff erosion, Coastal Engineering 2006: (In 5 Volumes). World Scientific, pp. 616-627.

Stein, R. and Macdonald, R. (2004) Organic Carbon Budget: Arctic Ocean vs. Global Ocean, The Organic Carbon Cycle in the Arctic Ocean. Springer, pp. 315-322.

Stroeve, J. and Notz, D. (2018) Changing state of Arctic sea ice across all seasons. Environmental Research Letters 13, 103001.

Terenzi, J., Jorgenson, M.T., Ely, C.R. and Giguère, N. (2014) Storm-surge flooding on the Yukon-Kuskokwim delta, Alaska. Arctic, 360-374.

The WAVEWATCH III ® Development Group (WW3DG) (2016) User manual and system documentation of WAVEWATCH III ® version 5.16. Tech.Note 329, NOAA/NWS/NCEP/MMAB, College Park, MD, USA, 326 pp.+ Appendices.

Thomson, J., Fan, Y., Stammerjohn, S., Stopa, J., Rogers, W.E., Girard-Ardhuin, F., Ardhuin, F., Shen, H., Perrie, W. and Shen, H. (2016) Emerging trends in the sea state of the Beaufort and Chukchi seas. Ocean Modelling 105, 1-12.

Thomson, J. and Rogers, W.E.J.G.R.L. (2014) Swell and sea in the emerging Arctic Ocean. 41, 3136-3140.

United States General Accounting Office (USGAO) (2014) Climate Change Adaptation: DOD can improve infrastructure planning and processes to better account for potential impacts. Report to Congressional Requesters

Van Vuuren, D.P., Edmonds, J., Kainuma, M., Riahi, K., Thomson, A., Hibbard, K., Hurtt, G.C., Kram, T., Krey, V. and Lamarque, J.-F. (2011) The representative concentration pathways: an overview. Climatic change 109, 5-31.

Vonk, J.E. and Gustafsson, Ö. (2013) Permafrost-carbon complexities. Nature Geoscience 6, 675-676.

Vonk, J.E., Sánchez-García, L., Van Dongen, B., Alling, V., Kosmach, D., Charkin, A., Semiletov, I.P., Dudarev, O.V., Shakhova, N. and Roos, P. (2012) Activation of old carbon by erosion of coastal and subsea permafrost in Arctic Siberia. Nature 489, 137-140.

Wegner, C., Bennett, K.E., de Vernal, A., Forwick, M., Fritz, M., Heikkilä, M., Łącka, M., Lantuit, H., Laska, M. and Moskalik, M. (2015) Variability in transport of terrigenous material on the shelves and the deep Arctic Ocean during the Holocene. Polar Research 34, 24964.

Weingartner, T.J., Danielson, S.L., Potter, R.A., Trefry, J.H., Mahoney, A., Savoie, M., Irvine, C. and Sousa, L. (2017) Circulation and water properties in the landfast ice zone of the Alaskan Beaufort Sea. Continental Shelf Research 148, 185-198.

Wicks, A.J. and Atkinson, D.E. (2017) Identification and classification of storm surge events at Red Dog Dock, Alaska, 2004–2014. Natural Hazards 86, 877-900.

Yager, G.C. and Ravens, T.M. (2013) Causeway Impacts on Sediment Transport in the Sagavanirktok River Delta, North Slope Alaska, ISCORD 2013: Planning for Sustainable Cold Regions, pp. 504-515.